Powder Technology 386 (2021) 335–349

Contents lists available at ScienceDirect

Powder Technology

journal homepage: www.elsevier.com/locate/powtec

Hydrodynamic dead zone in multiphase geophysical flows impacting a rigid obstacle

Yong Kong [a], Jidong Zhao [a,*], Xingyue Li [b]

[a] Department of Civil and Environmental Engineering, The Hong Kong University of Science and Technology, Hong Kong, China
[b] School of Architecture, Civil and Environmental Engineering, Swiss Federal Institute of Technology, Lausanne, Switzerland

ARTICLE INFO

Article history:
Received 7 October 2020
Received in revised form 1 March 2021
Accepted 22 March 2021
Available online 25 March 2021

Keywords:
Hydrodynamic dead zone
Multiphase geophysical flow
Fluid-particle interaction
Granular temperature
Unjammed-jammed transition

ABSTRACT

When a gravity-driven solid-fluid mixture, such as those in geophysical flows, hits a wall-like rigid obstacle, a metastable jammed zone called hydrodynamic dead zone (HDZ) may emerge. The unjammed-jammed transition of HDZ, controlled by the intricate interactions among the obstacle, the fluid and the solid of the flow, remains an open issue to be quantified for thorough understanding its underlying physics and mechanics. This study employs a coupled Computational Fluid Dynamics and Discrete Element Method (CFD-DEM) to examine the characteristics of HDZ formed when a geophysical flow comprised of gap-graded particles and a viscous liquid impacts an obstacle. To identify key features in the zonation of HDZ, a modified granular temperature is proposed considering the influences of inherent polydispersity and both translational and rotational motions of the particles in the impacting mixture. A source-sink model is further established to offer an interpretation of the nonlinear energy dissipation process during the unjammed-jammed transition of HDZ, where the modified granular temperature serves as a function of either time or distance. The structural anisotropy is found to serve as a good indicator for illuminating the flow-structure interaction transitions. Three regimes, namely, impact-up, roll-up and heap-up regimes, have been identified according to the statistical energy conversion and dissipation in the flowing layer upon the HDZ. The influence of particle rotation is found to be more significant in the dynamical exchange of HDZ when the impacting flow contains a wider polydispersity.

© 2021 Elsevier B.V. All rights reserved.

1. Introduction

When impeded by a barrier along its flow path, a solid-liquid mixture, such as those in typical geophysical flows, may undergo an unjammed-jammed transition evolving from a flow state into a quasi-static state to form a Hydrodynamic Dead Zone (HDZ). It exhibits a meta-stable internal structure with transient interstitial fluids that interacts intricately with the incoming flow and the impeding obstacle, resulting in the complicated run-up and overflowing patterns of perplexing physics. In physical terms, the formation of HDZ is a typical process experiencing unjammed-jammed transition [1–3]. Meanwhile, extensive experimental and numerical studies have demonstrated the formation of HDZ and its influence on operations in various industrial and natural processes, such as jet-induced jammed states [1,4,5], dry granular flow-wall interactions [2,6–11], stent-induced hemodynamics [12], pneumatic conveying [13] as well as mitigation of geophysical flows with rigid and flexible barriers [2,14–16]. Nonetheless, our current understanding of the zonation and key features of HDZ as well as associated physics remains preliminary, due partially to lack of robust and accurate descriptions of its spatial and temporal characteristics based on quantifiable data. For instance, Wendeler [16] estimated the impact load on a barrier based on a strongly idealized zonation of the HDZ, whose size is calculated according to the flow-channel basal friction angle. There are fundamental issues to be resolved pertaining to the quantification of mass and momentum exchange dynamics, energy dissipation, and the description of internal structure evolution in the unjammed-jammed transition of HDZ. Existing knowledge on HDZ has dominantly been derived from macroscopic observations, empirical predictions, and conceptual interpretations [14,16–18].

An accompanying issue in HDZ studies is the quantification of unjammed-jammed transition. Quantitative analyses of this transition of HDZ rely crucially on both feasible means to reproduce the physics with quantifiable results during the HDZ formation and accurate characterization of HDZ. Great efforts have been made towards understanding the behavior of unjammed-jammed transition in quasi-static or slow dry granular flows pertaining to the velocity [7], inertial number [19,20], density [21], the peak of contact force distribution [22], the vibrations [23], the shear stress [24], the friction [25], the mechanical entropy [26] and granular temperature [1,4,27]. There are, however, relatively scarce studies devoted to the characterization of HDZ in rapid multiphase debris flows, due possibly to certain key challenges.

* Corresponding author.
E-mail address: jzhao@ust.hk (J. Zhao).

https://doi.org/10.1016/j.powtec.2021.03.053
0032-5910/© 2021 Elsevier B.V. All rights reserved.

For instance, the calculations of density (or porosity) and entropy in a multiphase debris flow can be strongly affected by the phase content, fluid viscosity, and solid polydispersity. The contact-level information necessary for quantitative analyses, such as contact forces and configurational granular fluctuations, are not always available by conventional experimental tools or continuum-based numerical modeling approaches for rapid multiphase geophysical flows. Indeed, existing physical investigations on HDZ in geophysical flows have predominantly been based on monodisperse dry granular flow without consideration of the effects of the particle size distribution (PSD) and/or fluid-particle interactions [2,14,16,17]. Therefore, a reliable and quantitative means capable of describing the unjammed-jammed transition of HDZ in rapid geophysical flows is direly needed to address these challenges.

Granular temperature, a term first coined by Ogawa [28] and frequently mentioned in thermodynamics and statistical mechanics [29,30], has been commonly used for this purpose. It has been demonstrated that granular temperature is indicative of the transitivity of different states [1,4,30,31]. Song et al. [27] verified with experimental measurements the effectiveness of using granular temperature for the study of jammed granular materials in quasi-static flows. Sano and Hayakawa [4] confirmed the existence of an actual dead zone by streaming granular temperature in rapid dry granular flows. Nevertheless, other important factors, such as the effects of the Particle Size Distribution (PSD) and rotational motion of particles, have not been adequately considered. Indeed, the unjammed-jammed transition highly depends on the PSD in both quasi-static and rapid granular flows [4,21], especially for natural geophysical flows [32,33]. Campbell [29] and Lun [34] argued that the spin energy must be included in granular temperature to render a complete theory for the description of the motion of particles. However, to fully measure the rotational motions pose tremendous difficulties for experimentalists as far as a real 3D system is concerned. Most measurements thus far have been restricted to the vicinity of the walls [35,36]. More recent progress has been made in using magnetic resonance to measure the spatially resolved granular temperature [37,38]. Despite all these advances, it remains a challenge for experimental measurements to take account of the PSD and rotational motions of particles.

A solid-fluid mixture consisting of particles with a wide range of PSD exhibits remarkably more complex dynamics and phenomena compared to the aforementioned simplified cases, presenting challenges for quantifications and analyses. Conventional numerical modeling of geophysical flows is largely represented by continuum-based flow theories in conjunction with single-phase, two-phase [39] or three-phase fluids [40]. Meanwhile, particle-based methods including the DEM method [23,41], the Material Point Method (MPM) [42] and the Smooth Particle Hydrodynamics (SPH) [43–45] are popular for the modeling of flows. Indeed, as argued by Iverson [32], the prevailing continuum assumptions or pure particle-based modeling may underestimate the complexity caused by solid-fluid interactions in a multiphase geophysical flow. Consequently, the analysis of HDZ delineates a picture of the continuum-discrete modeling by exploiting the advantage of both continuum and discrete approaches. Different methods of flow dynamics modeling, such as the Computational Fluid Dynamics (CFD), the Lattice-Boltzmann Method (LBM), and SPH, have coupled with the DEM [46–49] for the said purposes. These varous methods have also been successfully applied to explore debris flows [48,49]. In this study, we employ a coupled discrete-continuum numerical approach to model the complicated multi-way interactions among the inflowing debris, the emerging HDZ, and the barrier. The CFD is coupled with the DEM to simulate the geophysical flow as a mixture comprised of gap-graded particles and viscous liquids. In Section 3, we demonstrate that the proposed method can reasonably capture the build-up of HDZ and the key debris-structure interactions. In Section 4, key features and underlying physics of the jammed region, the unjammed-jammed transition region as well as the flowing layer upon the HDZ will be examined based on the zonation of HDZ by a modified granular temperature.

2. Methodology: a coupled CFD-DEM for multiphase geophysical flow

The coupled CFD-DEM method is capable of capturing the complicated fluid-solid interactions in various engineering conditions, such as debris flows flowing into a reservoir [50], debris flows flowing over a natural terrain [51], as well as debris flows impacting on rigid and flexible structures [52,53]. It has been benchmarked with classic problems in the soil and fluid mechanics including conical sand piling in water [46] and dam break involving two non-Newtonian fluids mixed with particles [47]. Detailed benchmarks will be not repeated here to avoid excessive distractions. For the convenience of reference, the following provides a brief introduction of the coupled approach. Interested readers may refer to [46,47] for detail.

2.1. Governing equations for the fluid and the solid

The fluid phase (i.e., air and viscous liquid composed of water and fine-solid materials) in a geophysical flow is simulated by discretized fluid cells by CFD. The following continuity equation and locally averaged Navier-Stokes equation are solved for each fluid cell [54]:

$$\frac{\partial\left(\varepsilon_f\rho_f\right)}{\partial t}+\nabla\cdot\left(\varepsilon_f\rho_f\mathbf{U}^f\right)=0 \tag{1}$$

$$\frac{\partial\left(\varepsilon_f\rho_f\mathbf{U}_f\right)}{\partial t}+\nabla\cdot\left(\varepsilon_f\rho_f\mathbf{U}^f\mathbf{U}^f\right)=-\nabla p-\mathbf{f}^p+\varepsilon_f\nabla\cdot\boldsymbol{\tau}+\varepsilon_f\rho_f\mathbf{g}+\mathbf{f}^s \tag{2}$$

where $\mathbf{U}^f$ and p are the averaged velocity and pressure for fluid phase in a cell, respectively. $\mathbf{g}$ is the body force vector. ε_f denotes the void fraction. $\mathbf{f}^p=-\sum_{i=1}^{m}\mathbf{F}_i^f/V_c$ is the averaged volumetric interaction force imposed by particle(s) inside the fluid cell with cell volume V_c. The surface tension force $\mathbf{f}^s$ is based on the Continuum Surface Force (CSF) model [55] and is calculated by an *interDyMFoam* solver [46]. The three-dimensional expressions of stress tensor $\boldsymbol{\tau}$ for Newtonian and non-Newtonian fluids are reduced to the following functions. The following constitutive equation is assumed to govern a Newtonian fluid:

$$\tau=\mu_f\,\dot{\gamma} \tag{3}$$

where τ, μ_f, $\dot{\gamma}$ are the shear stress, viscosity, shear rate of the fluid, respectively. Compared to water as the fluid phase [46,52], the viscous-plastic slurry is treated as a more complicated non-Newtonian fluid modeled with the Herschel-Bulkley model [56]:

$$\tau=\tau_0+\kappa\dot{\gamma}\,\mathrm{n} \tag{4}$$

where τ_0 and κ are the yield stress and consistency index of the fluid, respectively. n is the flow index of the fluid. $n>1$ gives a shear-thickening fluid while $n<1$ corresponds to a shear-thinning fluid. $n=1$ leads to a Bingham fluid [57].

The particle phase in a geophysical flow is modeled by DEM [41,58] to solve the following Newton's equations governing the translational and rotational motion of each particle i:

$$m_i\frac{d\mathbf{U}_i^p}{dt}=\sum_{j=1}^{n_i^c}\mathbf{F}_{ij}^c+\mathbf{F}_i^f+\mathbf{F}_i^g \tag{5}$$

$$I_i\frac{d\boldsymbol{\omega}_i}{dt}=\sum_{j=1}^{n_i^c}\left(\mathbf{M}_{t,ij}+\mathbf{M}_{r,ij}\right) \tag{6}$$

where m_i and I_i are the mass and momentum of inertia of particle i, respectively. $\mathbf{U}_i^p$ and $\boldsymbol{\omega}_i$ denote the translational and angular velocities of

particle i, respectively. n_i^c is the total number of contacts for particle i. $\mathbf{F}_{ij}^c$, $\mathbf{M}_{t,ij}$ and $\mathbf{M}_{r,ij}$ are the contact force, tangential torque and rolling torque imposed on particle i from particle j or the walls, respectively. $\mathbf{F}_i^f$ is the fluid-particle interaction force acting on the particle i. $\mathbf{F}_i^g$ is the gravitational force acting on the particle i.

2.2. Fluid-particle interactions and coupling scheme

The fluid-particle interactions are considered by exchanging interaction forces $\mathbf{F}^f$ between the CFD and DEM computations. Four interaction forces are considered, including buoyancy force $\mathbf{F}^b$, drag force $\mathbf{F}^d$, virtual mass force $\mathbf{F}^{vm}$ and viscous force $\mathbf{F}^v$ [46,59]:

$$\mathbf{F}^f = \mathbf{F}^d + \mathbf{F}^b + \mathbf{F}^{vm} + \mathbf{F}^v \tag{7}$$

Details of these interactions forces can be found in Appendix A and literature [46,59–61].

Fig. 1 illustrates the coupling scheme between CFD and DEM. The solid phase in a geophysical flow mixture is simulated as gap-graded polydisperse particles by DEM. The fluid phase, comprised of fines and liquid in the flow, is modeled as a continuous viscous fluid phase by CFD. The coupling module is developed based on three open-source software platforms, namely: OpenFOAM [62] for CFD, LIGGGHTS [63] for DEM and CFDEM [64] for the coupling engine. This coupling engine later extended by [46,50,52] can exchange the interaction forces and other information between CFD and DEM (Fig. 1). A sequential iterative procedure rather than a concurrent scheme is followed for the solution. At each time step, the DEM solver first provides such information as the velocities and positions of particles i, j and k (see Fig. 1). The positions of all particles are then matched with the fluid cells to calculate relevant information of each cell such as the porosity and assembled momentum source term $\mathbf{f}^p = -(\mathbf{F}_i^f + \mathbf{F}_j^f + \mathbf{F}_k^f)/V_c$. With all state variables (e.g. averaged velocity and pressure) for each fluid cell solved by the CFD solver, the particle-fluid interaction forces $\mathbf{F}_i^f$, $\mathbf{F}_j^f$and $\mathbf{F}_k^f$ acting on the centroid of particle i, j and k are then updated and transferred back to the DEM to solve the particle system for the next time step. Detailed solution procedures can be found in [46].

3. CFD-DEM simulation of a solid-fluid mixture impacting on a rigid barrier

3.1. Computational model setup

Fig. 2 shows the model setup and an initial mixture sample. A gravity-driven mixture of viscous liquid and grains is first generated behind a valve wall before being released to an inclined slope to impact a rigid barrier (Fig. 2a). Key geometry and model parameters are summarized in Table 1. Fig. 2b shows a representative part of the initial packing with tri-disperse particles. In the lower part of Fig. 2b, we use the interparticle contact force structure instead of contacted particles to show the initial packing at zero kinetic granular temperature state. The contact force network is more homogenous in comparison with the internal structure of HDZ in the subsequent sections. For a better visibility, the force chain thickness has been magnified around 10 times. The sidewalls, channel bed, and barrier are idealized as rigid walls with a modulus ten times of that of grains.

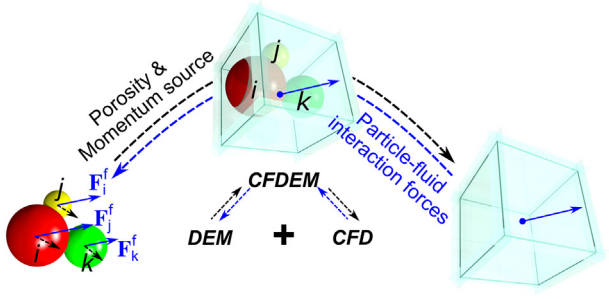

Fig. 1. The solution of coupled CFD-DEM modeling of geophysical flows. The solid phase is modeled as particles by the DEM and the fluid phase is modeled as a viscous fluid phase by the CFD. CFDEM refers to the computing engine enabling the exchange of interaction forces and other key information between the DEM and CFD.

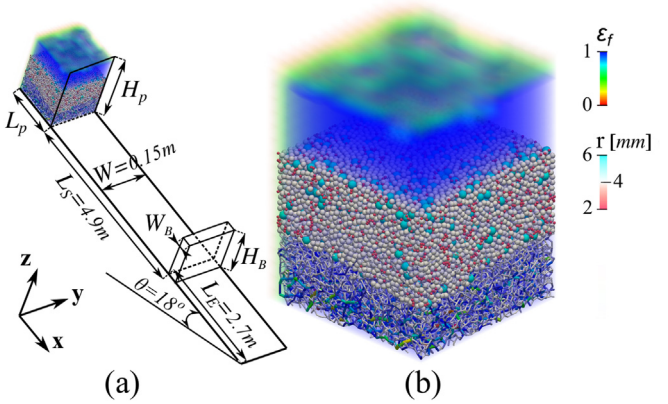

Fig. 2. Model set-up for coupled CFD-DEM simulation of gravity-driven multiphase geophysical flows impacting on a rigid barrier. (a): Model geometry prior to the release of the mixture; (b): Illustration of an initial sample of a particle-liquid mixture where the bottom layer is shown by the interparticle contact force network instead of these granular particles.

Real geophysical flows may contain soils with a wide range of grain sizes, from fines to big boulders [32]. The inherent polydispersity of a geophysical flow affects its mobility and the unjammed-jammed transition in the formation of the HDZ. To capture the effect of grain size polydispersity, four particle packings with identical volume are employed in the following cases: i) monodisperse cases ***M*** and ***DM***; ii) bi-disperse case ***B1***, with the mass percentages of particles with radius $r = 2$ mm and particles with $r = 6$ mm being 15% and 85%, respectively; iii) bi-disperse case ***B2***, with mass percentages of particles with $r = 4$ mm and particles with r = 12 mm being 50% and 50%, respectively; iv) tri-disperse case ***T*** (Fig. 2b), where the mass percentages for particles with radii equal to 2 mm, 4 mm and 6 mm are 5%, 10% and 85%, respectively. The DEM time step in this study has been adopted based on the constraint of Rayleigh time [66]. The CFD time step is dertermined according to the coupling interval between CFD and DEM. Following [53], we exchange information between CFD and DEM computations every 100 time steps of DEM to ensure balanced accuracy and efficiency in this study. Hence, the CFD time step is set to 100 times of the DEM time step. The total computing time for each case of 10 s flow and debris-structure interactions, on a 4-core Intel CPU (3.2 GHz) desktop computer, is around 7 to 12 days.

3.2. Build-up of HDZ: numerical simulation versus experimental observation

It is instructive to first compare the numerical simulation with experimental observations on HDZ. To render them comparable, the Froude similarity should be ensured between the experimental tests and numerical simulations. Froude number N_{Fr} has been widely used as a dimensionless number in studying the impact of geophysical flows onto a barrier structure [14,15]. It is defined as:

$$N_{Fr} = v/\sqrt{\mathbf{g}h\cos\theta} \tag{8}$$

where v and h are the velocity and thickness of incoming flow, respectively. Fig. 3a, b and c shows the formation process of a mechanical stable HDZ formed at the upstream of the rigid barrier during the

Table 1
Model parameters adopted for the coupled CFD-DEM simulations.

Categories	Variables	Values	Categories	Variables	Values
Debris particle	N_p (cases ***M*** & ***DM***)	44,088; $r = 4$ mm	Air	ρ_f [kg/m^3]	1
	N_p (case ***B1***)	64,009; $r = 2, 6$ mm		μ_f [Pa·s]	1.48×10^{-5}
	N_p(case ***B2***)	22,860; $r = 4, 12$ mm	Liquid	ρ_f[a] [kg/m^3]	1600
	N_p (case ***T***)	32,495; $r = 2, 4, 6$ mm		κ[a] [Pa·s^n]	90
	ρ_s # [kg/m^3]	2650		n[a]	0.34
	r [mm]	2, 4, 6, 12		τ_0[a] [Pa]	180
	E_{p-w} # [GPa]	700	Geometry (sample and barrier)	H_B [m]	0.12
	E_{p-p} # [GPa]	70		W_B [m]	0.045
	ϑ #	0.3		H_p [m]	0.5628
	e #	0.4		L_p [m]	0.4
	μ_r #	0.15	Simulation control	Δt (DEM) [s]	5×10^{-7}
	μ_{p-p} #	0.7		Δt (CFD) [s]	5×10^{-5}
	μ_{p-w} #	0.5		Real time [s]	10

Notes: E, ϑ and e denote Young's modulus, Poisson's ratio and restitution coefficient, respectively; N_p, r *and* ρ_s are the total number, radius and density of particles, respectively; The subscripts or superscript 'p - p' and 'p - w' indicate the interparticle and particle-wall properties, respectively; # refers to typical values of physical properties for geophysical flows summarized by [32,47].
[a] Refers to the typical values of a Herschel-Bulkley fluid [65].

simulation of case ***M***, in comparison with photographs (Fig. 3d, e and f) taken by Song [67]. Specifically, the pre-impact N_{Fr} of the flume test [67] on solid-liquid mixture flow impacting on a rigid barrier using centrifuge modeling is equal to 3.6, which is consistent with case ***M***. This N_{Fr} is also a typical value of geophysical flows in the field [14]. The numerical predictions of three stages in the formation of HDZ are qualitatively consistent with the experimental observations [67]. As shown in Fig. 3a, b and c, three typical stages can be identified during the build-up of the HDZ. Stage *I* (Fig. 3a) features the front impact of the geophysical flow onto the rigid barrier, causing a jet perpendicular to the channel bottom and helping to form an HDZ along the upstream surface of the barrier. As shown in Fig. 3d, this impact process was also observed in the experiment [67]. In stage *II* (Fig. 3b), the jet flow rapidly dissipates to become a reflected wave and an overflow passing the barrier. The HDZ in stage *II* is impacted by both the collapse of the reflected wave and the incoming debris. After the reflected wave fully collapses, the incoming flow continues to impact on the HDZ at stage *III* (Fig. 3c), contributing to a growing HDZ.

In addition to Froude number, the barrier/flow height ratio (i.e. H_B/h) may have a notable influence on the formation, shape and development of HDZ as well as the dominated impact mechanisms (i.e. runup and pile-up) [2,6,14]. Indeed, Faug [2] found that both N_{Fr} and H_B/h may control the dynamic patterns associating dead zone and the shapes of dead zones during the impact of dry granular flows on the wall. In this study, the ratio H_B/h is around 2.5, indicating that the presented simulations are in an intermediate regime [2] between the steady granular

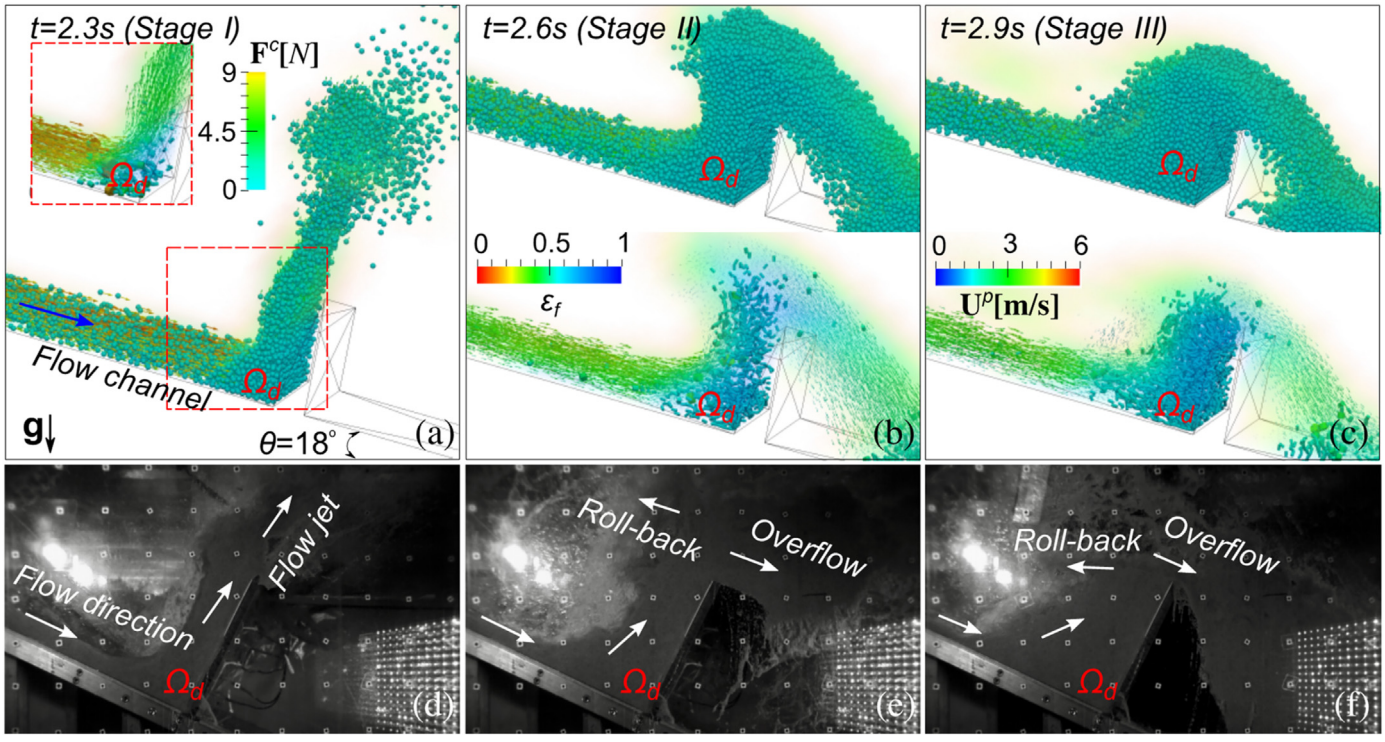

Fig. 3. Numerical simulations (a, b & c) and experimental observations in flume tests by Song [67] (d, e & f) on key debris-structure interactions during the impact of geophysical flow (with similar pre-impact Froude number) on a rigid barrier. Three stages are identified: (*I*) from frontal impact to form flow jet (a & d), (*II*) recirculation and overflow (b & e), and (*III*) run up and further overflow (c & f). The tubes and arrows in the insets of (a-c) represent the interparticle contact force ($\mathbf{F}^C$) networks and velocity ($\mathbf{U}^p$) vectors, respectively. Ω_d indicates a broad domain of HDZ formed along the upstream of the rigid barrier to be further treated in the sequel.

dead zone regime (lower H_B/h) and the unsteady granular jump regime (higher H_B/h) [2]. To highlight the influence of the interstitial fluid on the impact process, a comparison of the key flow-barrier interactions between the wet case ***M*** and a reference dry case ***DM*** with similar pre-impact conditions (e.g. $N_{Fr} \cong 3.5$, $H_B/h \cong 2.5$) has been included in Appendix B.

3.3. Profiles of the HDZ

Fig. 4 shows the profile of the HDZ during the formation process. The HDZ is shown in Fig. 4a in terms of interparticle contact force network, fluid fraction ε_f and particle velocity $\mathbf{U}^p$. There is an identifiable region in front of the barrier where the granular particles form a quasi-static contact structure wherein the interparticle contact forces restrict all particles from moving, presenting a mechanically stable dead zone. This zone is subjected to continuous dynamic impact by the incoming flow,

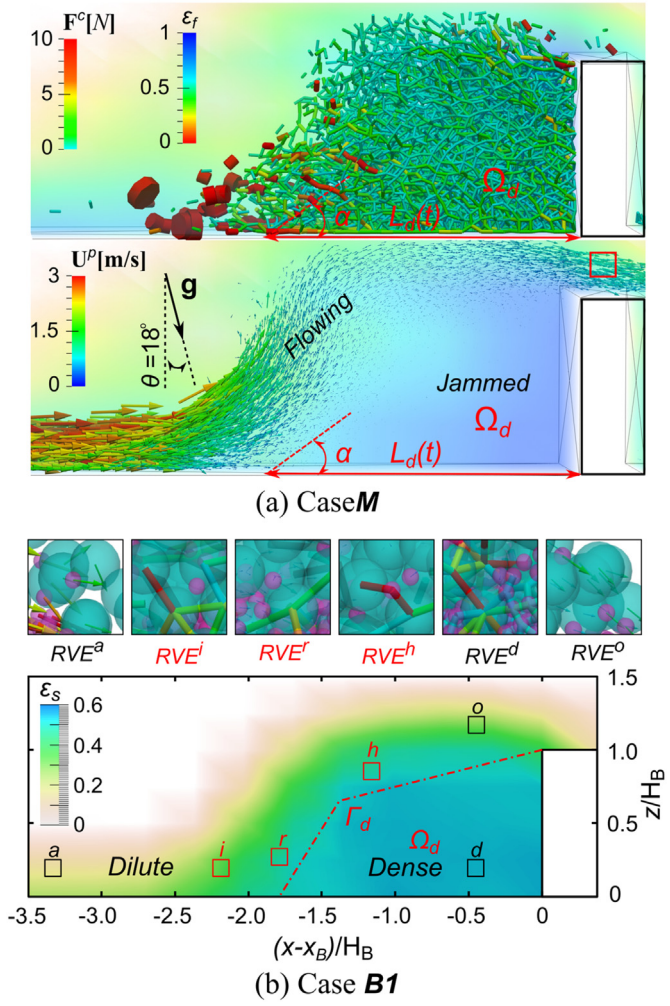

Fig. 4. Key profiles including contact structure and velocity, as well as fluid and solid fractions associated with the HDZ for (a) case ***M*** and (b) case ***B1*** at 3 s. Six sampling windows (typically one fluid cell in the CFD) as Representative Volume Elements (RVEs) associated with the HDZ as demonstrated in (b). $\mathbf{U}^p$ and $\mathbf{F}^c$ denote the particle velocity and interparticle contact vectors, respectively. The arrows indicate the magnitude and direction of particle velocities. The bars indicate the contact force chains whose thickness are magnified around 10 times to render visibility in (a). ε_f and ε_s indicate the fluid volume fraction (background in a) and solid volume concentration (background in b), respectively. α and $L_d(t)$ respectively denote the time-dependent impact angle and length of HDZ (see Section 4.2). The dash-dotted red lines in (b) represent an illustrative boundary of the HDZ.

which is transmitted through an established network of interparticle contacts (the bar-like structure in the upper panel of Fig. 4a) also used in dry granular flows [7]. The barrier can feel both the static and dynamic loads transferred through the network. Faug et al. [7] found that the normal force on the obstacle is characterized by high-frequency fluctuations with high amplitudes due to a fluctuating force chain network inside the dead zone. The lower panel of Fig. 4a shows a flowing layer (shown as arrows) coexisting with a jammed HDZ, which has attracted numerous past studies [2,15].

Fig. 4b shows six sampling windows of the Representative Volume Elements (*RVEs*, shown as squares) which demonstrate the contact intensity and particle component in representative flow regimes during the unjammed-jammed transition process of HDZ, which include very dilute ($\varepsilon_s < 0.1$), dilute ($0.1 < \varepsilon_s < 0.5$) and dense ($0.5 < \varepsilon_s < 0.6$) regimes. The chosen sample windows, RVE^i, RVE^r and RVE^h, are three representative locations of the flowing layer upon the HDZ, which will be further discussed in Section 4.4. The internal structures shown in Fig. 4 reveal that the HDZ indeed exists dynamically. Indeed, the mechanically stable, solid-like characteristic of the HDZ may experience, partially or wholly, transient processes of relaxing, creeping, and flowing, casting uncertainties to the validity of the qualitative description of the unjammed-jammed transition in various situations. For instance, the stability of HDZ could be disturbed by the approaching rollover surges or soliton-like waves in geophysical flows [27,59]. A new index as proposed below will be proposed to quantify and analyze the metastable HDZ.

4. Signatures of the hydrodynamic dead zone

4.1. A modified granular temperature for the zonation of HDZ

4.1.1. Modified granular temperature

The granular temperature has been commonly used to quantify the state of granular flow [1,4]. Campbell [29] attributed two mechanisms to granular temperature: the kinetic granular temperature T_s by the migration of particles and the collisional granular temperature T_c based on the momentum transfer by collision. Specifically, T_s is applicable for characterizing geophysical flows from very dilute ($\varepsilon_s < 0.1$) to dense ($0.5 < \varepsilon_s < 0.59$) regimes, which covers typical regimes when an unjammed-jammed transition occurs (Fig. 4b) in geophysical flows. T_c is regarded unsuitable to describe dilute flows [68] where forces exerted by the fluid and gravity dominate over interparticle collisions on the motion of particles.

The original concept of granular temperature [28] is defined as $T = \langle u' \rangle$, where u' and $\langle\rangle$ are the instantaneous deviation from the mean velocity and an appropriate average, respectively. In this study, a modified granular temperature is proposed to further consider the inherent polydispersity [4,21] and the rotational motion [29,34] of the particles in the flow. Consider particles i ($i = 1 \sim N_r$) with mass m_i, translational velocity $\mathbf{u}_i$ and rotational velocity $\boldsymbol{\omega}_i$ and located in the calculating cell with its central point $\mathbf{r}$. A modified coarse-grained function of T_s for rapid debris flows are defined according to the following additive superposition of the translational and rotational components:

$$T_s(\mathbf{r}) = \frac{1}{DN_{\mathbf{r}} \sum_{i \in N_{\mathbf{r}}} m_i} \sum_{i \in N_{\mathbf{r}}} \left(m_i u_i'^2 + \mathrm{I}_i \omega_i'^2 \right) \tag{9}$$

where $N_{\mathbf{r}}$ denotes the total number of particles of the calculating cell with a central point $\mathbf{r}$. D denotes the spatial dimension (i.e. $D = 3$). The moment of inertia for a spherical particle i is calculated by $I_i = 2m_i r_i^2/5$, where m_i and r_i represent respectively the mass and radius of particle i. $\mathrm{u}_i' = \|\mathbf{u}_i\| - \langle \mathbf{u}(\mathbf{r}) \rangle$ and $\omega_i' = \|\boldsymbol{\omega}_i\| - \langle \boldsymbol{\omega}(\mathbf{r}) \rangle$ are instantaneous deviations of the translational velocity $\|\mathbf{u}_i\|$ and the rotational velocity $\|\boldsymbol{\omega}_i\|$ for particle i from its mean velocities of $\langle \mathbf{u}(\mathbf{r}) \rangle$ and $\langle \boldsymbol{\omega}(\mathbf{r}) \rangle$ located in the calculating cell, respectively.

The averaged translational and rotational solid velocities of all particles located in the cell with central point **r** are determined by:

$$\langle \mathbf{u}(\mathbf{r}) \rangle = \frac{\mathbf{1}}{N_\mathbf{r}} \sum_{i}^{N_\mathbf{r}} |\mathbf{u}_i| \tag{10}$$

$$\langle \boldsymbol{\omega}(\mathbf{r}) \rangle = \frac{\mathbf{1}}{N_\mathbf{r}} \sum_{i}^{N_\mathbf{r}} |\boldsymbol{\omega}_i| \tag{11}$$

The translational granular temperature $T_t(\mathbf{r})$ and rotational granular temperature $T_r(\mathbf{r})$ for the cell can be respectively expressed as:

$$T_t(\mathbf{r}) = \frac{1}{DN_\mathbf{r} \sum_{i \in N_\mathbf{r}} m_i} \sum_{i \in N_\mathbf{r}} \left(m_i u_i^2 \right) \tag{12}$$

$$T_r(\mathbf{r}) = \frac{1}{DN_\mathbf{r} \sum_{i \in N_\mathbf{r}} m_i} \sum_{i \in N_\mathbf{r}} \left(\mathrm{I}_i \omega_i^2 \right) \tag{13}$$

Herein we adopt the moving average coarse-graining method to calculate the granular temperature with a moving length $\Delta x = \Delta z = Max\,[2r_i]$ during a short time duration of Δt = 5e-6 s (i.e. 10 DEM steps) from our computation.

4.1.2. Zonation of HDZ based on the modified granular temperature

Bouquet et al. [31] reported that the jamming-to-flowing transition is driven by a coupling between mean and fluctuating velocity, whereas Faug et al. [7] observed a threshold value (i.e. 0.05) of the normalized velocity for the determination of dead zone in dry granular flows. Sano and Hayakawa [4] further confirmed the existence of the dead zone with a granular temperature $T \cong 0$. In this study, a threshold of normalized granular temperature $T_s^N = T_s / max\,[T_s] = 10^{-3}$ is assumed to bound the region (i.e. Γ_d) of HDZ. Analogously, $T_t^N = T_t / max\,[T_t]$ and $T_r^N = T_r / max\,[T_r]$ denote the normalized translational and rotational granular temperature, respectively. Any analyzing location with T_s^N, T_t^N and T_r^N below their threshold value (i.e. 10^{-3}) is regarded within an HDZ. Note that the decomposed granular temperatures are not normalized according to the same normalizer as the modified granular temperature. Fig. 5 presents the zonation of HDZ for the monodisperse case ***M*** and the bi-disperse case ***B1*** according to the contours of the three normalized and modified granular temperature quantities.

While the zonation of HDZ by the three granular temperatures appears to be largely similar from Fig. 5, there are certain observable differences. Zoning according to the map of T_s^N shares more similarity with that of T_t^N instead of T_r^N for both cases, due to higher contribution by translational components in the overall granular temperature T_s^N. Indeed, the maximum and average values of T_t for both cases are much higher than those of T_r, indicating that the kinetic energy induced by the translational motion shows higher fluctuations than its rotational counterpart. It is also notable that both the maximum and average T_t and T_r for case ***B1*** are much larger than those for case ***M*** (Fig. 5a, b, d and e), indicating the polydispersity indeed helps to enhance the mobility of granular particles in geophysical flows in both translational and

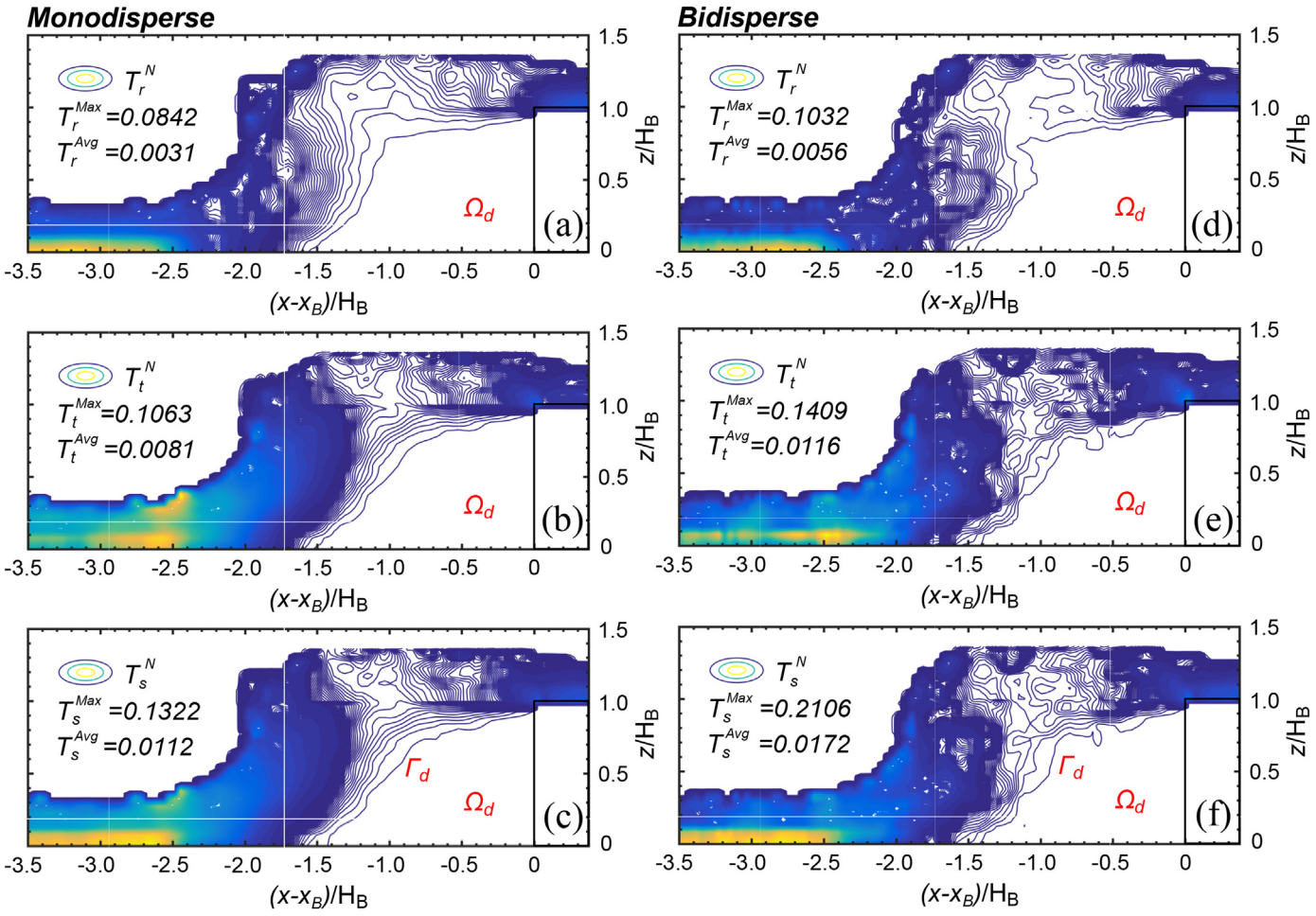

Fig. 5. Maps of three normalized granular temperatures (i.e. rotational T_r^N, translational T_t^N and modified T_s^N) associated with HDZ for geophysical flow impacting a rigid barrier with cases ***M*** and ***B1*** in the *xz*-plane at 3.5 s. (a), (b) and (c) show the T_r^N, T_t^N and T_s^N for case ***M***, respectively. (d), (e) and (f) show the T_r, T_t and T_s for case ***B1***, respectively. The boundaries of HDZ, Γ_d, are represented by the contours of normalized granular temperatures T_r^N, T_t^N and T_s^N equal to 10^{-3}.

rotational degrees. Also noticed is the boundary of HDZ in case ***B1*** being more uneven than case ***M*** (Fig. 5c and f).

Furthermore, the contribution by the rotational component takes a substantial weight in both cases that cannot be neglected. The mean rotational granular temperature T_r^{Avg} in case ***B1*** accounts for a high proportion of about 32.5% and it is 27.6% in case ***M***. This depicts that material polydispersity can enhance the importance of rotational granular temperature on the modified granular temperature. In reality, a natural debris flow may involve particles of more irregular in shape and much wider in grain size range, both helping to significantly promote grain rotations and enhance the role of rotational fluctuating kinetic energy. Fig. 5c and f also show the bottom region before the HDZ between $(x - x_B)/H_B =$ [-3.5, −2.5] with a much higher T_s that is consistent with reported observations [69,70]. This high T_s coincidently agrees with that of T_r in Fig. 5a and d, indicating the significance to include rotation in the consideration of granular temperature in Eq. (9). Indeed, rough channel beds can provide additional sources to promote fluctuating kinetic energies through collisions and slips [71], which enhance the rotational granular temperature. In addition to the wet cases, the zonation of dead zone for the reference dry case ***DM*** with the same dead zone length as the wet case ***M*** has been examined in Appendix B.

4.2. Structural characteristics of HDZ

4.2.1. Dynamic nature of the jammed HDZ

Quantifying the structural characteristics of HDZ helps to measure the impact force, the energy dissipation, and the outflow discharge of geophysical flows over a barrier [2,6,8,9,15,17]. A major challenge lies in the temporal and spatial variations of HDZ. Simplified boundary of HDZ, e.g., by single or two straight lines as shown in Fig. 4b (dashed lines), has been proposed in past studies [2,8,15] for derivation of impact models and estimation of impact force on a rigid barrier [7,17]. In this study, the normalized and modified granular temperature T_s^N is employed to measure the impact angle α and the length L_d of HDZ. L_d is determined as the distance between the upstream front of the barrier and the intersection point between the HDZ surface boundary Γ_d and the channel bed (Fig. 6a). α is defined as the angle between the channel bed and the red straight dash lines obtained based on the intersection of the channel bed with the best fitting line of one incoming flow depth of the HDZ boundary Γ_d. Fig. 6b shows the temporal evolutions of α for cases ***M***, ***B1,*** and ***T***, in comparison with the reference dry case ***DM*** (i.e. pre-imapct $N_{Fr} \cong 3.5$, $H_B/h \cong 2.5$) and a special case of dry sand flow as measured by Law [72], which shows notable differences. The measured mean α in the dry sand flow by Law [72] is much larger than that measured in the dry case ***DM***, due to the steeper slope angle (i.e. $\theta = 35°$) adopted by Law [72] as compared to the dry case ***DM*** (i.e. $\theta = 18°$). The mixture cases of geophysical flow demonstrate an interesting temporal evolution of impact angle in contrast with the generally monotonic development of dry flows, revealing the significant effect of the fluid phase in the mixtures. In all three mixture cases, the impact angle invariably increases during the debris-structure interaction stage *I* and reaches a peak at stage *II*, followed by a decay in stage *III*. The peak impact angle is mainly induced by the unique recirculation behavior for the mixture cases (see Fig. 3b) where the corresponding time t/t_0 for cases ***M***, ***B1,*** and ***T*** are respectively 0.275, 0.25, and 0.25. Note that the recirculation may also occur to dry granular flows if the slope is sufficiently steep [2]. The decrease of impact angle in stage *III* is due to the use of surge flows instead of continuous flows for the incoming flows in our simulations. It is noticed that the shape of HDZ and thus the impact angle may be affected by the barrier/flow height ratio H_B/h and the flow discharge [2,6–8], which requires further investigation for solid-fluid mixtures in the future.

4.2.2. Structural signatures of transitions in flow-structure interactions

Observable macroscopic responses have been a focus by most existing studies on the flow-structure interactions [14–17]. It is instructive to offer a microscopic correlation for these macroscopic observations. The spatial distribution of contact force orientations associated with the time-dependent HDZ can characterize the different impact behaviors of flow-structure interactions. Fig. 7 shows the directional rose diagram of the contact fabric anisotropy intensity ξ_C defined as the total number of contacts within a specified angle interval (see details in Appendix C) pertaining to the signature of HDZ during the impact process. Specifically, the inner contact fabric structure of HDZ presents three apparent directional spikes or poles during the impact process for all three cases ***M***, ***B1*** and ***T***. The blue dotted lines with empty triangles (Fig. 7a, c and e) show the first spike evolves immediately upon the impact and flips slightly from the positive *x*-axis (i.e. flow direction) with $\delta_i = \xi_C^I$ during stage *I* when the impact is dominated by dynamic loads exerted by the arriving surge flow. The second spike emerges

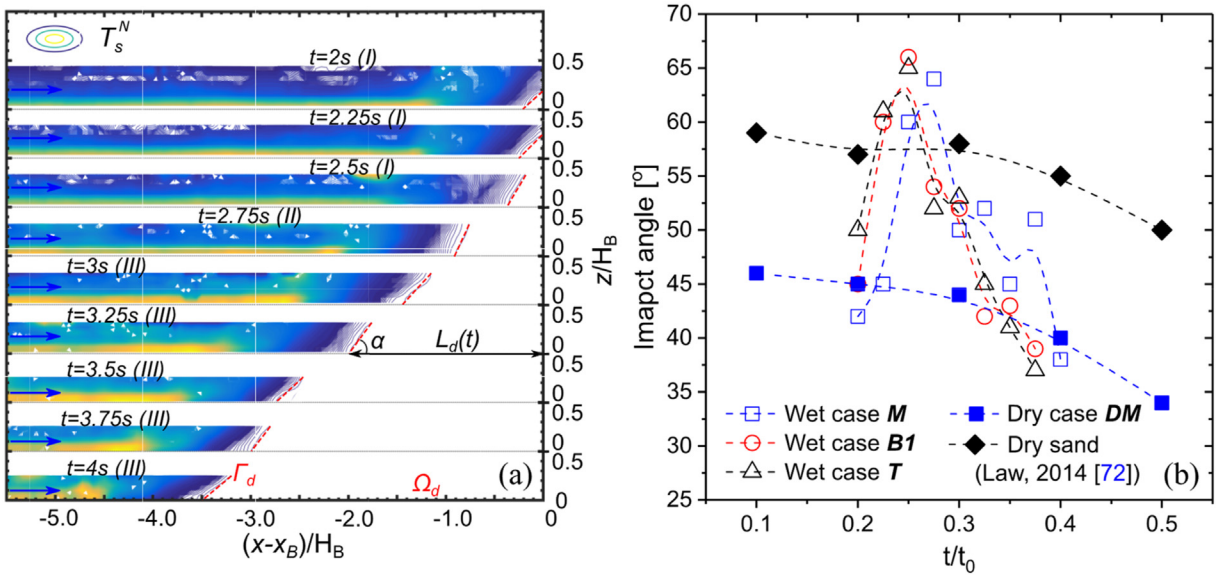

Fig. 6. (a) Illustration of measurement of the impact angle α and length $L_d(t)$ of HDZ for case ***M*** based on the flow depth *h* and normalized granular temperature T_s^N. (b) Temporal evolutions of impact angle α for cases ***DM***, ***M***, ***B1,*** and ***T***, where t_0 is the total time (10 s) for the respective case ***M***.

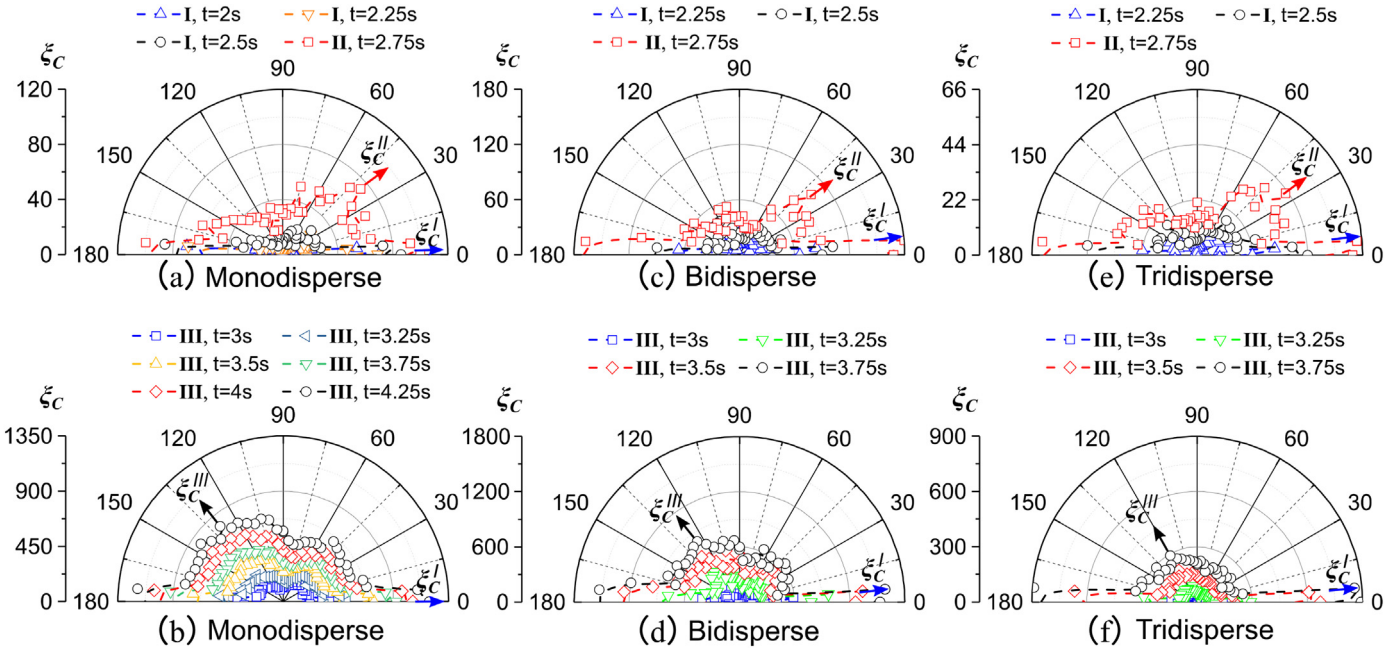

Fig. 7. Evolution of contact fabric anisotropy intensity ξ_c associated with the time-dependent HDZ. The blue, red, and black arrows represent directional spikes for stage *I*, stage *II*, and stage *III* in the impact process, respectively. (a), (c) and (e) denote stages *I* and *II* for cases ***M***, ***B1*** and ***T***, and (b), (d) and (f) represent stage *III* for cases ***M***, ***B1,*** and ***T***, respectively.

with $\delta_i = \xi_C^{II}$ along an angle of 40°, signifying the beginning of stage *II* when the recirculation and overflow processes cause reorientations of the contact fabrics in the HDZ. The contacted particles rearrange themselves so that the contact forces close to the positive *x*-axis (horizontal flow direction) are significantly reduced due to the sudden change of governing impact mechanism or macroscopic behavior. The third spike flips from the *x*-direction to around 125° with $\delta_i = \xi_C^{III}$ in stage *III*, and the angle between ξ_C^{III} and ξ_C^{II} is close to 90 degrees, as shown in Fig. 7b, d and f. These three spikes of contact fabric anisotropy represent the major contact normal direction the emerging HDZ adjusts internally to resist the external forces during the impact process. Towards the end of stage *III*, a mechanically stable HDZ is gradually established and its inner structure becomes relatively homogeneous. The first indicator ξ_C^I persists, whilst the second indicator ξ_C^{II} disappears. Since the magnitude of ξ_C (radius length) correlates positively with the total particle number of the solid-liquid system associated with HDZ, ξ_C^I, ξ_C^{II} and ξ_C^{III} increases steadily with increased number of particles trapped in the progressive formation of HDZ.

4.3. Phase diagram for the unjammed-jammed transition

4.3.1. Spatio-temporal evolution of T_s

As a field state variable, T_s does not necessarily refer to an equilibrium state. Herein we consider an idealized case of scenario to explore key features pertaining to the unjammed-jammed transition for a solid-liquid system. We plot the values of T_s in the bottom layer (i.e. $z/H_B = 0.1$, Fig. 5c) to investigate the spatial evolution of T_s from unjammed to jammed state. Because the majority of particles in the bottom layer will be jammed in the HDZ while the particles in the surface layer of incoming flows will experience a much more complicated and varied journey. Fig. 8c shows spatially distributed granular temperature T_s in the bottom layer ($z/H_B = 0.1$) in the *xz*-plane for case ***M*** at $t = 3$ s. The fluctuating kinetic energy is found to flow from regions of higher T_s (or higher potential) to regions of lower T_s (lower potential) during a typical and idealized unjammed-jammed transition process. The kinetic theories provide the following definition of energy flux vector **q** for a dry granular flow [29,71]:

$$\mathbf{q} = -\epsilon \nabla T_s \tag{14}$$

as a measure of the conductive flux of T_s from highly agitated to less-agitated regions with a conductivity ϵ. The conductivity ϵ is given in terms of velocity ***u***, the T_s and the pair distribution at contact [71].

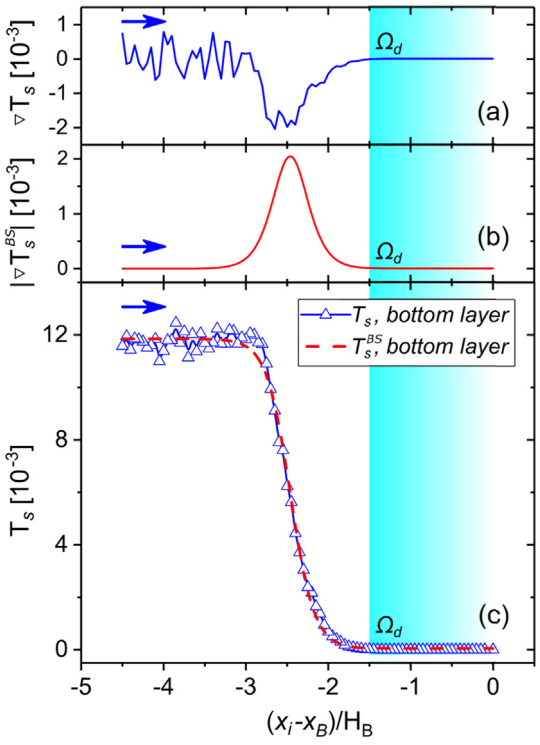

Fig. 8. Spatially distributed granular temperature T_s in the bottom layer ($z/H_B = 0.1$) in the *xz*-plane for case ***M*** at $t = 3$ s. The upper inset represents the gradient of the Bezier fit of T_s. The lower inset shows the absolute value of the gradient of the Boltzmann sigmoid fit (red dash line) for T_s. Note that the blue arrow indicates the flow direction. T_s^{BS} denotes the Boltzmann sigmoid fit of $T_s(x_i\text{-}x_B)$.

Fig. 8a presents the gradient of the Bezier fit of T_s, which indicates energy flux according to Eq. (14). Analogously, Fig. 8b shows the absolute value of the gradient of the Boltzmann sigmoid fit of T_s. The energy flux needs to be positive definite [32]:

$$|\mathbf{q}| = \left|-\lambda . e^{-\frac{(x-x_I)^2}{d}}\right| \propto |\nabla T_s| \tag{15}$$

wherein λ is a constant of usual thermal conductivity. x_I is the inflection point of the Boltzmann sigmoid distribution (red dashed line in Fig. 8c). d denotes the maximum value of the internal transport rate of T_s. Fig. 8b shows that the internal transport rates of T_s increases rapidly to a peak before dropping to zero during the unjammed-jammed transition process, and the energy states of both the incoming geophysical flow and the HDZ at the bottom layer are virtually stationary (i.e. $|\nabla T_s^{BS}(x_i - x_B)| \cong 0$). Meanwhile, Fig. 8a indicates that the fluctuations or 'noise' are much milder in the HDZ as compared with the free approaching flow. Interestingly, it is noticed that the effective friction (i.e. the ratio of normal stress to shear stress) exhibits a stronger fluctuating behavior in the dead zone as compared with the incoming flow region for dry granular flows [7]. The different dominant regions of the fluctuations in the granular temperature and the effective friction might be due to their distinct governing factors in definition, e.g., according to velocity variation and force/stress variation, respectively. The goodness-of-fit of the Boltzmann sigmoid model for the spatially distributed T_s along the bottom layer reaches greater than 0.99 for the R-square. Therefore, the Boltzmann sigmoid model is found suiting well for describing the spatially distributed granular temperature during the unjammed-jammed transition (Fig. 8c).

As shown in Fig. 9, we further compare the temporal distribution of T_s (t) during the unjammed-jammed transition process at three chosen locations, $z_i/H_B = 0.2$, $(x_i - x_B)/H_B = -1.0, -1.5$ and -2.0. $T_s(t)$ calculated in all three monitored cells shows a mild increase at the beginning and then undergoes a sharp decrease during the unjammed-jammed transition process (Fig. 9). At the beginning of the unjammed-jammed transition process for three locations, significant deviations between the T_s and their Boltzmann sigmoid fits have been observed due to the particles starting to undergo more intense collisions. The red empty triangles and red dash line in Fig. 9b experience another significant deviation between T_s and the Boltzmann sigmoid fit at around 2.75 s at the late stage of the unjammed-jammed transition. This unstable T_s is triggered by the impact of the reflected waves on the measuring location (i.e. $(x_i - x_B)/H_B = -1.5$) at stage *II* (i.e. recirculation and overflow). It is further observed that the temporal distribution of $T_s(t)$ at the given locations also follows the Boltzmann sigmoid model (Fig. 9b). The goodness-of-fit of the Boltzmann sigmoid model with R-Square values are 0.981, 0.967 and 0.915 for $(x_i\text{-}x_B)/H_B$ equal to −1.0, −1.5 and − 2.0, respectively. Fig. 9a presents the absolute value of the energy flux in Eq. (15) for the idealized Boltzmann sigmoid fit of $T_s(t)$ at the three chosen locations. The maximum rate of fluctuating kinetic energy dissipation increases when the monitored cell is closer to the rigid obstacle. As indicated in Figs. 8 and 9, the idealized Spatio-temporal evolution of the modified granular temperature undergoes an unjammed-jammed transition process that may follow the Boltzmann sigmoid model.

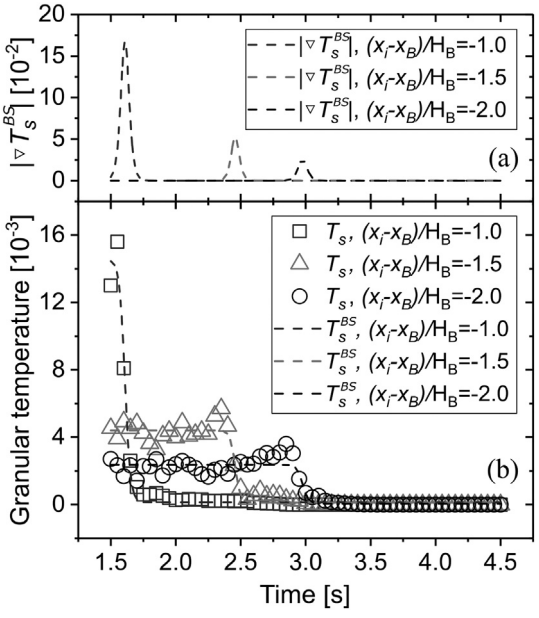

Fig. 9. Evolution of granular temperature $T_s(t)$ at three chosen locations, i.e., $z_i/H_B = 0.2$, $(x_i - x_B)/H_B = -1, -1.5$ and -2 for case ***M*** at $t = 3$ s. Dash lines in (a) are the absolute values of the gradient of T_s^{BS}, i.e., the Boltzmann sigmoid fit of T_s.

4.3.2. A conceptual source-sink model

The Boltzmann sigmoid model has been found relevant to a wide range of physics processes, such as sediment transport initiation [3], shock-wave structure in rarefied gas flows [73,74], supercooled liquids [75] and critical micelle concentration in chemistry [76]. Based on the analysis in preceding sections, the spatially distributed granular temperature T_s during the unjammed-jammed transition is further simplified as follows:

$$T_s(x) = T_s^{HDZ} + \frac{T_s^{DGI} - T_s^{HDZ}}{1 + exp\left[-(x - x_I)/d\right]} \tag{16}$$

wherein T_s^{DGI} and T_s^{HDZ} denote its fluctuating kinetic energy at the dynamical grain-inertia (DGI) and quasi-static regions, respectively. The T_s^{HDZ} is infinitely close to zero in this study. In addition, the energy dissipation profile of the unjammed-jammed transition can be quantified by transition thickness and asymmetry (see Appendix D, [73,77]).

Base on the results of a representative case ***M*** from Fig. 8c, Fig. 10 is plotted to demonstrate the conceptual diagram of T_s during the unjammed-jammed transition process. The $|\nabla T_s|$ denotes the energy flux of fluctuating kinetic energy. Notably, the fluctuating kinetic energy flux flows from the highly agitated regime (i.e. free approaching debris) to a less-agitated regime (i.e. HDZ) during the unjammed-jammed transition process in geophysical flow impacting a rigid obstacle. Specifically, at the dynamical grain-inertia regime ($x < x_{DGI}$), $|\nabla T_s| \to 0$, indicating that the energy state is relatively stationary. Post to the DGI regime, the internal transport rate of energy flux gradually increases to a peak before decreasing to almost zero during the unjammed-jammed transition process. As shown in Fig. 10, the left half after the DGI regime of the spatial

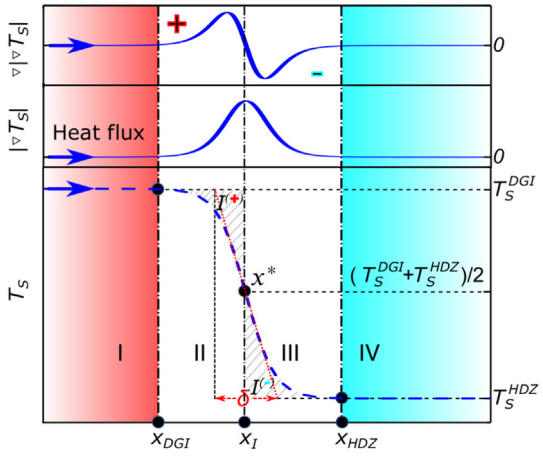

Fig. 10. Conceptual diagram of the unjammed-jammed transition process based on the spatial distribution of T_s. The black dot x^* marks the position of the steepest gradient which is linearly extrapolated to provide the transition thickness δ. The transition asymmetry, $Q = I^{(-)}/I^{(+)}$, follows from the ratio of the two integrals (shaded regions) of the lower and upper half of the profile of T_s.

distributions of $|\nabla T_s|$ with $\nabla|\nabla T_s| > 0$ is called 'Source' regime (marked by +) while the right side of the spatial distributions of $|\nabla T_s|$ with $\nabla|\nabla T_s| < 0$ is called 'Sink' regime (marked as -) [74,78]. The final $T_s^{HDZ} \to 0$ limit produces a mechanically stable region with $|\nabla T_s| \to 0$, corresponding to a quasi-static region with zero fluctuating kinetic energy. Hence, we propose the following four sub-regimes to describe the unjammed-jammed transition process associated with HDZ: I) Dynamical grain-inertia regime with $x < x_{DGI}$ and $|\nabla T_s| \to 0$; II) Source regime with $x_{DGI} < x < x_I$, $\nabla|\nabla T_s| > 0$ and an increasing $|\nabla T_s|$; III) Sink regime with $x_I < x < x_{HDZ}$, $\nabla|\nabla T_s| < 0$ and a decreasing $|\nabla T_s|$; IV) Hydrodynamic dead zone with $x_{HDZ} < x$, $T_s^{HDZ} \to 0$ and $|\nabla T_s| \to 0$.

The above provides a generalized source-sink model to conceptually describe the nonlinear energy dissipation process during the unjammed-jammed transition process. Despite that the coarse-graining distribution of T_s in the simulated unjammed-jammed transition may not be rigorous enough, it is both theoretically and experimentally identifiable. Further experimental data of geophysical flows is needed to substantiate the proposed modified granular temperature and its thermodynamic significance. Specifically, the kinetic theories experience difficulties in describing solid-liquid flows, due probably to addressing the energy conversion between solid and fluid phase interactions [32]. Granular temperature itself is a manifest of the interactions between particles and the interstitial fluid. Furthermore, significant collisional frictional and rotational motions of particles in geophysical flows require the consideration of balance equations for angular momentum and the energy of the fluctuations in particle spin [34,71,79], which poses challenges for practical measurement. Nonetheless, the presented model and results constitute a step forward in this direction. In addition to the polydispersity and rotational motion considered in this study, other factors, such as solid fraction, flow discharge and dynamics, H_B/h, and particle shape, may affect the unjammed-jammed transition and can be examined for further modification and improvement of the source-sink model.

4.4. Key regimes of the flowing layer upon the HDZ

Quantifying the energy dissipation and conversion in the flowing layer upon the HDZ bears important scientific and engineering significance. However, the widely adopted quantifiers on energy or contact properties for the entire solid system, such as kinetic energy and coordinate number, are not appropriate to be analyzed. It is also instructive to incorporate the role played by rotational kinetic energy E_k^r and fluid-particle interactions. Inspired by the Positron Emission Particle Tracking (PEPT) method adopted in opaque flows [80], we monitor a specified group of particles with labeled IDs during a short time (i.e. from $t = 3.9975$ s to $t = 4$ s) located above the barrier (red square in Fig. 4a). Specifically, we trace 20 particles with $r = 4$ mm in case ***M***, 20 particles with $r = 4$ mm and 15 particles with $r = 12$ mm in case ***B2*** to calculate the statistical average quantities. These quantities are assigned to an equivalent particle i to represent a typical particle in the flowing layer upon HDZ. Note that the relative potential energy ΔE_p is calculated by $\Delta E_p = mg(z\cos\theta - x\sin\theta)|_{t=4}^{t}$, where x and z are the statistical average quantities of the labeled particles.

As shown in Fig. 11, z/H_B denoted by the red dash line shows that the equivalent particle i in the flowing layer undergoes the flow-structure interaction during stage *III* (run up and overflow). The statistical values of E_k^t are higher than those of E_k^r, indicating that more kinetic energy is stored in the translational mode than in its rotational counterpart. A bi-disperse packing in case ***B2*** has an averaged E_k^t which is around five times of E_k^r (Fig. 11a and b), while in the monodisperse case ***M***, $E_k^t = 0.0025$ kg·m^2/s^2 is more than ten times larger than $E_k^r = 0.0002$ kg·m^2/s^2 in the approaching geophysical flows at $t = 2$ s (Fig. 11c). Hence, the neglection of E_k^r in the calculation of total kinetic energy may incur notable error, especially for realistic geophysical flows with inherent polydispersity. Furthermore, the majority of energy dissipated during the run-up process bounded by two vertical dash lines (Fig. 11). Noted that RVE^i, RVE^r and RVE^h are the three representative locations in the flowing layer (Fig. 4b). As shown in Fig. 11, these RVEs can be distinctively identified according

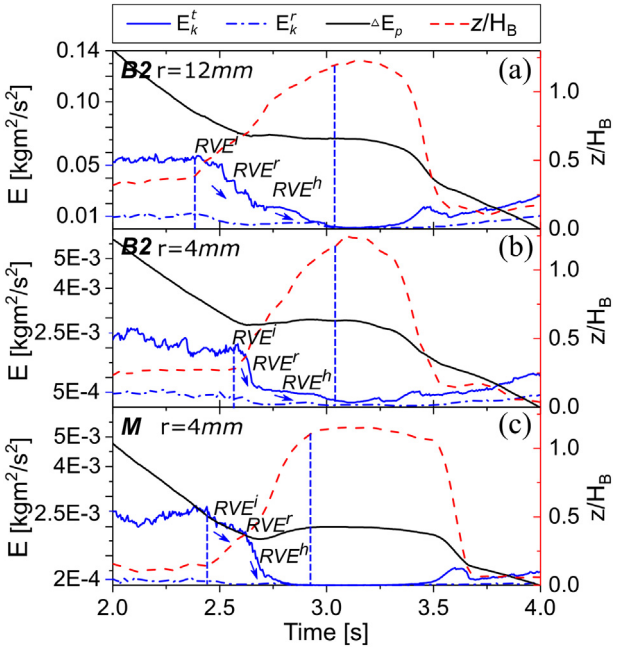

Fig. 11. Spatial and temporal evolutions of translational kinetic energy E_k^t, rotational kinetic energy E_k^r and relative potential energy ΔE_p of an equivalent particle i in the flowing layer. (a), (b) and (c) represent case ***B2*** with $r = 4$ mm, case ***B2*** with $r = 12$ mm and case ***M*** with $r = 4$ mm, respectively. E_k^t, E_k^r and ΔE_p are denoted by blue solid lines, blue dash-dotted lines, and black solid lines, respectively. The red dash line represents the z coordinate normalized by the barrier height.

to the evolutions of ΔE_p (black solid lines) and E_k^t (blue lines). Specifically, the blue arrows denote two clear regimes of the flowing layer with different energy dissipation rates of E_k^t. Interestingly, the energy dissipation rate for E_k^t in RVE^i is substantially lower than in RVE^r for case ***M*** (Fig. 11c), while they are similar for case ***B2*** (Fig. 11a and b). Moreover, most kinetic energy (> 90%) for cases ***M*** and ***B2*** in stage *III* is dissipated in the flowing layer upon the HDZ from the simulitons.

The accumulated energy dissipation for the labeled particle i at time t is defined as $E_d = (E_k^t + E_k^r + E_p)|_{t=2}^{t}$. It depicts the addition of kinetic and potential energy at t relative to $t = 2$ s. Fig. 12a, c and e shows two peaks for the energy dissipation rate represented by red arrows. Particle-fluid interaction forces also play an important role in energy dissipation, in addition to interparticle collisions. Intuitively, when the particle flow arrives close to the HDZ at around $t = 2.7$ s, the energy dissipation rate reaches the first peak. The fluid-particle interaction forces $\mathbf{F}^f$ acting on the statistical particle along the z and x directions show increasing and decreasing trends, respectively, which lead to positive values of $\mathbf{F}_z^f$ and negative values of $\mathbf{F}_x^f$. This indicates that the $\mathbf{F}^f$ serves as a driving force for the upward motion and an impeding force for the forward motion during this stage. Meanwhile, the absolute values of both $\mathbf{F}_z^f$ and $\mathbf{F}_x^f$ increase to their respective peak before dropping to a normal level. Accordingly, the intensities of both the driving force for the upward motion and the resistance force for the forward motion experience the first increase and then decrease. The second peak of energy dissipation rate is associated with the free-fall debris impacting the channel which is not our focus. Interestingly, as shown in Fig. 12b, d and f, E_k^t keeps decreasing during $t = 2.5$– 3.0 s, whilst E_k^r shows a decreasing-increasing-decreasing trend during the flow climbing onto the top of HDZ (at around $t = 2.5$–3.0 s). The mild increase of E_k^r (represented by blue arrows in Fig. 12b, d and f) occurring at around $t = 2.6$ s, $t = 2.75$ s and $t = 2.7$ s respectively in the three cases. This maybe related to the energy transfer from E_k^t to E_k^r [81], interparticle collisions and particle-fluid interactions.

Based on the above analyses, three key regimes in the flowing layer (red squares in Fig. 4b) of the HDZ are identified: i) the frontal impact-up regime represented by RVE^i; ii) the roll-up regime represented by RVE^r; iii) the heap-up regime represented by RVE^h. These regimes correspond

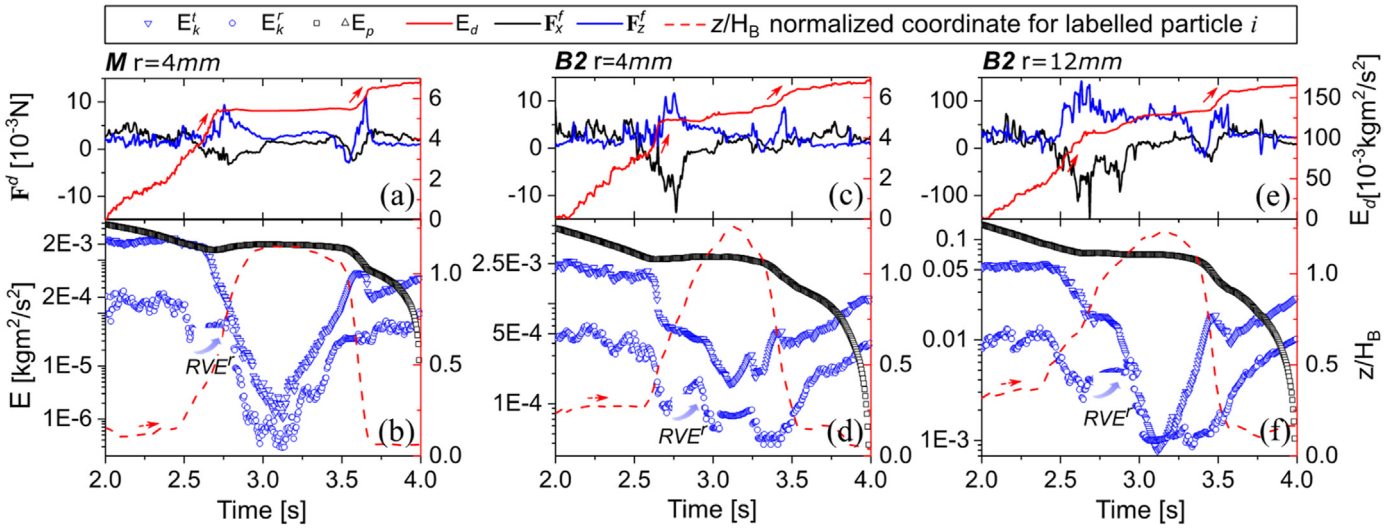

Fig. 12. Energy conversion and dissipation of an equivalent particle *i* for case ***M*** and case ***B2*** in the flowing layer. The blue lines and black lines in (a), (c), and (e) represent the total fluid-particle interaction forces expressed in Eq. (7) along *x* direction($\mathbf{F}_x^f$) and *z* direction ($\mathbf{F}_z^f$), respectively. E_k^t, E_k^r and ΔE_p are the translational energy, rotational energy, and potential energy, denoted by blue triangles, blue circles, and black squares in (b), (d), and (f), respectively. The red solid lines in (a), (c) and (e) illustrate the accumulated energy dissipation E_d.

to both spatially and temporally distributed flow zones with distinct dominated mechanisms identifiable by an statistically equivalent particle *i* in the flowing layer. Take the case in Fig. 12b as an example, the translational and rotational energies decrease from $t = 2.4$– 2.6 s, during which the impact-up regime is identified. From $t = 2.6$– 2.75 s, the translational energy decreases while the rotational kinetic energy increases, which corresponds to the roll-up regime. From $t = 2.75$– 3.0 s, both the translational and rotational energies decrease again, marking the occurrence of a heap-up regime. After $t = 3.0$ s, both the translational and rotational energies increase, and an overflow regime takes place.

5. Conclusions

The characteristics of hydrodynamic dead zone formed during multiphase geophysical flows impacting on a rigid obstacle have been numerically investigated based on coupled CFD-DEM simulations. The study highlights the complicated nature of the Hydrodynamic Dead Zone (HDZ) involving intricate mechanisms arising from the multiphase and multiscale origins of the solid-fluid mixture flow, and emphasizes the necessity of using powerful tools to capture the strong solid-fluid interactions (such as the coupled CFD-DEM approach employed) and proper quantifiers to identify and analyze the dynamic and transitional nature of HDZ. The study offers the following new findings on HDZ.

(1) A modified granular temperature T_s has been proposed to consider the effects of grain polydispersity and both rotational and translational motions of particles in a geophysical flow, based on which distinctive features in the zonation of HDZ can be quantitatively identified. It is demonstrated that during the formation of HDZ, the rotational component accounts for a high proportion in both the fluctuating kinetic energy and the kinetic energy, and its contribution becomes higher when the grain polydispersity is further considered. The rotational motion of the particles in a multiphase geophysical flow thus plays a critical role in the structure evolution and dynamical exchange of the HDZ. This effect is considered more significant for a natural geophysical flow when the irregular grain shape and wider polydispersity further promote particle rotations.

(2) Using the T_s as a measure, a generalized source-sink model has been proposed to characterize the nonlinear energy dissipation process in unjammed-jammed transitions, where the T_s can be a function of either time or distance. The Boltzmann sigmoid equation is found to fit our data for the generalized source-sink model well. Based on this model, four sub-regimes are further proposed to furnish a complete description of a typical unjammed-jammed transition process during the emergence of HDZ: the dynamic grain inertia regime, source, sink, and the HDZ regime. Transition thickness and asymmetry can also be introduced to characterize the energy dissipation profile of such a process.

(3) This study further offers a macro-micro correlation on the characterization of HDZ, based on microscopic structural anisotropy of contact force network formed within the solid particles in the HDZ. It is found that the structural anisotropy may serve as a good indicator for illuminating the macroscopic transitions of key flow-structure interactions. Three regimes that define the flowing layer upon HDZ, namely, impact-up, roll-up, and heap-up regimes, have been further identified according to the statistical energy conversion and dissipation.

The new insights revealed from this study offer improved understanding and quantification of the unjammed-jammed transition process, which may not only help our understanding of gravity driven geophysical flows for natural hazard mitigations, but also offer potentials in improving the efficiency for a wide range of practical industrial processes, including pneumatic conveying and others.

CRediT authorship contribution statement

Yong Kong: Methodology, Software, Data curation, Writing - original draft. **Jidong Zhao**: Conceptualization, Methodology, Supervision, Writing - review & editing. **Xingyue Li**: Software, Visualization, Writing - review & editing.

Declaration of Competing Interest

The authors declare no competing interest.

Acknowledgments

The research reported in this study was financially supported by the National Natural Science Foundation of China (Project #11972030) and the University Grants Council of Hong Kong (RGC/GRF Project #16205418, TBRS Project #T22-603/15N and CRF Project #C6012-15G). All data used to generate figures of the study can be found from the following link: https://figshare.com/s/d9cbed962f7a82b854ae.

Appendix A. Fluid-particle interaction forces

When a particle accelerates or decelerates in a fluid, it needs to deflect a certain volume of the surrounding fluid to move through and hence generates extra virtual inertia to the system. The virtual mass force is an interaction force to account for this effect and is defined by [50]:

$$\mathbf{F}^{vm} = C_{vm}\rho_f V_i^p\left(\dot{\mathbf{U}}_i^p - \dot{\mathbf{U}}^f\right)/2 \tag{A1}$$

where the virtual mass coefficient $C_{vm} = 2.1 - 0.132/(0.12 + A_c), A_c = (\mathbf{U}^p - \mathbf{U}^f)^2/[(\dot{\mathbf{U}}_i^p - \dot{\mathbf{U}}^f)2r_i]$. V_i^p is the volume of the particle i. $\dot{\mathbf{U}}_i^p$ and $\dot{\mathbf{U}}^f$ are the accelerations of the particle i and the fluid cell, respectively. In addition, the viscous force acting on particle i is induced by the deviatoric stress tensor and is defined by [59]:

$$\mathbf{F}^v = -(\nabla\cdot\boldsymbol{\tau})V_i^p \tag{A2}$$

The average density based buoyancy force acting on the considered particle i with radius r_i [60] is:

$$\mathbf{F}^b = \frac{4}{3}\pi\rho_f r_i^3\mathbf{g} \tag{A3}$$

The drag force proposed by Di Felice [61] is adopted:

$$\begin{cases} \mathbf{F}^{\mathrm{d}} = \dfrac{1}{2}C_d\pi\rho_f r_i^2\left(\mathbf{U}^{\mathrm{f}} - \mathbf{U}^{\mathrm{p}}\right)\left|\mathbf{U}^{\mathrm{f}} - \mathbf{U}^{\mathrm{p}}\right|\varepsilon^{1-\chi}, \\ C_d = \left(0.63 + \dfrac{4.8}{\sqrt{Re_p}}\right)^2, \\ Re_p = \dfrac{2\varepsilon_f\rho_f r_i\left|\mathbf{U}^{\mathrm{f}} - \mathbf{U}^{\mathrm{p}}\right|}{\mu}, \\ \chi = 3.7 - 0.65\,exp\left[-\dfrac{(1.5 - log_{10}Re_p)^2}{2}\right] \end{cases} \tag{A4}$$

where C_d is the particle-fluid drag coefficient depending on the particle Reynolds number Re_p. $\varepsilon^{1-\chi}$ denotes a corrective function that accounts for the effect of other particles in the system on the drag force of the considered particle i.

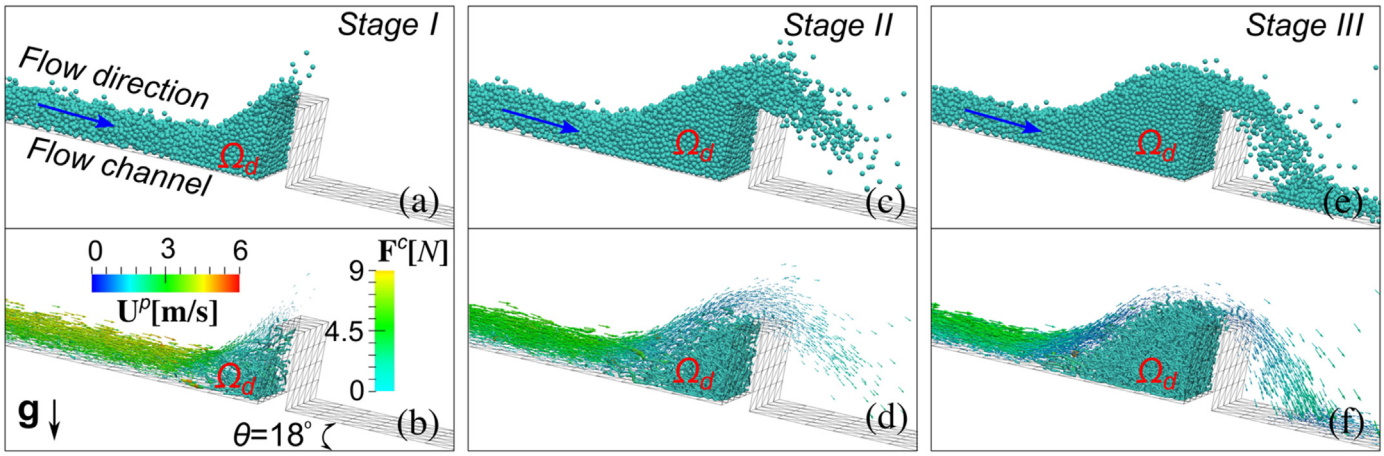

Fig. A1. Numerical observations on key debris-structure interactions during the impact of dry granular flow (i.e. pre-imapct $N_{Fr} \cong 3.5$, $H_B/h \cong 2.5$) on a rigid barrier with case ***DM***. Three stages are identified: (*I*) frontal impact (a & b), (*II*) run up and first overflow (c & d), and (*III*) run up and further overflow (e & f). See Fig. 3 for the detailed caption.

Appendix B. Influences of interstitial fluid on the patterns of dead zone

Demarcating between the role of interstitial fluid and frictional particles in a solid-fluid mixture experiences difficulties due to the complicated fluid-paritlce energy conversion and interactions [32,33]. To further clarify the role of the fluid phase, we have simulated a reference dry case ***DM*** with similar pre-impact conditions (e.g. $N_{Fr} \cong 3.5$, $H_B/h \cong 2.5$) to the wet case ***M***. Fig. A1 shows the three key flow-barrier interactions for the dry case ***DM***. By comparing the mixture case ***M*** (Fig. 3a) with the dry case ***DM*** (Fig. A1), it is found that the interstitial fluid plays a crucial role in changing the key flow-barrier interactions and dynamic patterns of dead zones. The jet flow formed at stage *I* and the recirculation behavior at stage *II* are only observed from the mixture case ***M*** (Fig. 3), and disappear in the dry case ***DM*** (Fig. A1). This indicates that the interstitial fluid prevails at stages *I* and *II*. On the other hand, both the dry and wet cases demonstrate more stabilized contact networks and dynamic patterns of dead zone at impact stage *III*, as shown in Figs. 3c and A1f, reflecting the dominance of the granular skeleton (or particles) at stage *III* for both cases.

The surrounding fluid may influence the impact process according to two key mechanisms: i) Increasing the kinematic energy of particles by imposing driving force to the particles, and reducing inter-particle contact forces and therefore energy dissipation from shearing among grains by applying buoyancy to the particles [82]; ii) Reducing the energy dissipated via shearing between the flowing layer materials and the jammed HDZ. Specifically, the energy of mixture flow is mainly dissipated via the roll-back waves towards subsequent flow [82,83], whereas the energy of dry granular flow is mainly dissipated via shearing between the flowing layer and jammed dead zone [17,82].

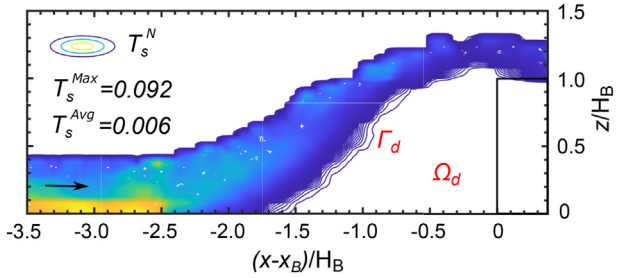

Fig. A2. Maps of normalized granular temperatures (i.e. T_s^N) associated with dead zone for dry granular flow (i.e. pre-imapct $N_{Fr} \cong 3.5$, $H_B/h \cong 2.5$, $\theta = 18°$) impacting a rigid barrier with case ***DM*** in the *xz*-plane at stage *III*. Note that the length of dead zone in the dry case ***DM*** is consistent with the wet case ***M*** in Fig. 5c. See Fig. 5 for the detailed caption.

Fig. A2 shows the zonation of dead zone by the proposed granular temperature for the dry case ***DM***, whose dead zone length is consistent with the wet case ***M***. By comparing the dead zone between the mixture case ***M*** (see Fig. 5c in Section 4.1.2) and the dry case ***DM*** (Fig. A2), we found that the flowing layer upon the dead zone for the dry case is much thinner than that for the wet case. It is due possibly to the large shearing between the flowing layer and the dead zone in the dry case, which decelerates the flowing particles and transfers more particles to the dead zone. Note that both the maximum and average values of the measured granular temperatures for the wet case ***M*** are much larger than the dry case ***DM***. Meanwhile, both the dry and wet cases experience a much higher T_s at the bottom region before the HDZ between $(x - x_B)/H_B = [-3.5, -2.5]$, which is mainly due to the channel beds providing additional sources to promote fluctuating kinetic energies through collisions and slips in the free approching flows [71].

Appendix C. Contact fabric anisotropy intensity

The contact fabric anisotropy intensity ξ_C is defined as the statistical summation of the number of contacts with angle δ_i within a specified angle interval $[\gamma, \gamma + 5)$. δ_i denotes the angle between the contact force orientation of $\mathbf{F}_i^c$ projected onto the *xz*-plane and the positive *x*-axis. $\gamma \in [0, 5, 10 \cdots 175]$ are gap-graded constants that divide a semi-circular plane into 36 equal parts. The length and height of the statistical zone are $L_d(t)$ (see Fig. 6) and H_B, respectively. Hence, ξ_C could be calculated by the characteristic function:

$$\xi_C(\gamma) = \sum_{i=1}^{n} \chi_{(\gamma,\gamma+5)}(\delta_i, \gamma), \tag{A5}$$

$$\chi_{(\gamma,\gamma+5)}(\delta_i, \gamma) = \begin{cases} 1, \delta_i \in [\gamma, \gamma + 5) \\ 0, \delta_i \notin [\gamma, \gamma + 5) \end{cases}, \tag{A6}$$

where n denotes the total number of contacts in the statistical domain associated with the time-dependent HDZ. For instance, $\xi_C(25) = 62$ implies the summation of the number of contacts with angles (δ_i, projected onto the *xz*-plane) within an angle interval [25,30].

Appendix D. Transition thickness and asymmetry of the source-sink model

To minimize the complexity, it is instructive to define the energy dissipation profile such as the unjammed-jammed transition with a few key parameters. Indeed, Fig. 10 has depicted two most often used profile characteristics, transition thickness and asymmetry [64,69]. The so-called transition thickness [64] is defined as follows:

$$\delta = \frac{T_s^{DGI} - T_s^{HDZ}}{\max\left(\frac{\partial T_s}{\partial x}\right)}, \tag{A7}$$

by assuming a linear connection between the T_s before and behind the unjammed-jammed transition with a slope corresponding to the steepest gradient of T_s. In this study, we assume the transition thickness starts with $|\nabla T_s| \to 0$, approaches a maximum internal transport rate of energy flux $|\nabla T_s|$ and finally decreases slowly to $|\nabla T_s| \to 0$. This non-monotonic behavior represents an interplay between steepening nonlinearity and smoothing dissipation. Moreover, the transition asymmetry [64,69] is defined as:

$$Q = \frac{I^{(-)}}{I^{(+)}} = \frac{\int_{x_{HDZ}}^{x^*} \left(T_s(x^*) - T_s^{HDZ}\right) dx}{\int_{x^*}^{x_{DGI}} \left(T_s^{DGI} - T_s(x^*)\right) dx}, \tag{A8}$$

where the characteristic position x^* is determined by $T_s(x^*) = (T_s^{DGI} + T_s^{HDZ})/2$. The transition asymmetry offers more information on the actual shape of the profile than the transition thickness does. The transition asymmetry Q is found larger than 1 in this study based on the calculation of the Boltzmann sigmoid fit in Fig. 8c. This indicates that the unjammed-jammed transition is a relatively slower relaxation process beyond the position characteristic x^*. Note that typical values of the shock asymmetry lie between 0.8 and 1.2 for rarefied gas flows [64].

References

[1] J. Ellowitz, H. Turlier, N. Guttenberg, W.W. Zhang, S.R. Nagel, Still water: dead zones and collimated ejecta from the impact of granular jets, Phys. Rev. Lett. 111 (16) (2013) 168001.
[2] T. Faug, Depth-averaged analytic solutions for free-surface granular flows impacting rigid walls down inclines, Phys. Rev. E 92 (6) (2015), 062310, .
[3] T. Pähtz, A.H. Clark, M. Valyrakis, O. Durán, The physics of sediment transport initiation, cessation, and entrainment across aeolian and fluvial environments, Rev. Geophys. 58 (1) (2020) (e2019RG000679).
[4] T.G. Sano, H. Hayakawa, Jet-induced jammed states of granular jet impacts, Prog. Theor. Exp. Phys. 2013 (10) (2013), 103J02, .
[5] D. Su, Y.X. Wang, Y.J. Huang, A.M. Zsaki, Granular jet composed of elliptical particles impacting a fixed target, Powder Technol. 313 (2017) 303–311.
[6] T. Faug, P. Lachamp, M. Naaim, Experimental investigation on steady granular flows interacting with an obstacle down an inclined channel: study of the dead zone upstream from the obstacle. Application to interaction between dense snow avalanches and defence structures, Nat. Hazard Earth Syst. 2 (3/4) (2002) 187–191.
[7] T. Faug, R. Beguin, B. Chanut, Mean steady granular force on a wall overflowed by free-surface gravity-driven dense flows, Phys. Rev. E 80 (2) (2009), 021305, .
[8] B. Chanut, T. Faug, M. Naaim, Time-varying force from dense granular avalanches on a wall, Phys. Rev. E 82 (4) (2010), 041302, .
[9] T. Faug, P. Caccamo, B. Chanut, Equation for the force experienced by a wall overflowed by a granular avalanche: experimental verification, Phys. Rev. E 84 (5) (2011), 051301, .
[10] T. Faug, P. Childs, E. Wyburn, I. Einav, Standing jumps in shallow granular flows down smooth inclines, Phys. Fluids 27 (7) (2015), 073304, .
[11] A. Albaba, S. Lambert, T. Faug, Dry granular avalanche impact force on a rigid wall: analytic shock solution versus discrete element simulations, Phys. Rev. E 97 (5) (2018), 052903, .
[12] J.M. Jiménez, P.F. Davies, Hemodynamically driven stent strut design, Ann. Biomed. Eng. 37 (8) (2009) 1483–1494.
[13] F. Yan, A. Rinoshika, Application of high-speed PIV and image processing to measuring particle velocity and concentration in a horizontal pneumatic conveying with dune model, Powder Technol. 208 (1) (2011) 158–165.
[14] C.W.W. Ng, C.E. Choi, R.C.H. Koo, G.R. Goodwin, D. Song, J.S.H. Kwan, Dry granular flow interaction with dual-barrier systems, Géotechnique 68 (5) (2017) 386–399.
[15] D. Song, C.W.W. Ng, C.E. Choi, G.G. Zhou, J.S.H. Kwan, R.C.H. Koo, Influence of debris flow solid fraction on rigid barrier impact, Can. Geotech. J. 54 (10) (2017) 1421–1434.
[16] C. Wendeler, Debris-Flow Protection Systems for Mountain Torrents: Basics Principles for Planning and Calculation of Flexible Barriers, Swiss Federal Institute for Forest, Snow and Landscape Research WSL, 2016 187–188.
[17] W. Ashwood, O. Hungr, Estimating total resisting force in flexible barrier impacted by a granular avalanche using physical and numerical modeling, Can. Geotech. J. 53 (10) (2016) 1700–1717.
[18] S.B. Savage, The mechanics of rapid granular flows, Advances in Applied Mechanics, 24, Elsevier 1984, pp. 289–366.
[19] P. Jop, Y. Forterre, O. Pouliquen, A constitutive law for dense granular flows, Nature 441 (7094) (2006) 727.
[20] G.D.R. MiDi, On dense granular flows, Eur. Phys. J. E 14 (4) (2004) 341–365.
[21] S. Luding, Granular matter: so much for the jamming point, Nature Phys. 12 (6) (2016) 531.
[22] E.I. Corwin, H.M. Jaeger, S.R. Nagel, Structural signature of jamming in granular media, Nature 435 (7045) (2005) 1075–1078.
[23] N. Gaudel, S.K. De Richter, Effect of vibrations on granular material flows down an inclined plane using DEM simulations, Powder Technol. 346 (2019) 256–264.
[24] D. Bi, J. Zhang, B. Chakraborty, R.P. Behringer, Jamming by shear, Nature 480 (7377) (2011) 355.
[25] H.A. Vinutha, S. Sastry, Disentangling the role of structure and friction in shear jamming, Nat. Phys. 12 (6) (2016) 578.
[26] A.H.W. Ngan, Mechanical analog of temperature for the description of force distribution in static granular packings, Phys. Rev. E 68 (1) (2003), 011301, .
[27] C. Song, P. Wang, H.A. Makse, Experimental measurement of an effective temperature for jammed granular materials, Proc. Natl. Acad. Sci. 102 (7) (2005) 2299–2304.
[28] S. Ogawa, Multitemperature theory of granular materials, Proc. of the US-Japan Seminar on Continuum Mechanical and Statistical Approaches in the Mechanics of Granular Materials, Gakajutsu Bunken Fukyu-Kai 1978, pp. 208–217.
[29] C.S. Campbell, Rapid granular flows, Annu. Rev. Fluid Mech. 22 (1) (1990) 57–90.
[30] J. Casas-Vázquez, D. Jou, Temperature in non-equilibrium states: a review of open problems and current proposals, Rep. Prog. Phys. 66 (11) (2003) 1937.
[31] L. Bocquet, J. Errami, T.C. Lubensky, Hydrodynamic model for a dynamical jammed-to-flowing transition in gravity driven granular media, Phys. Rev. Lett. 89 (18) (2002) 184301.
[32] R.M. Iverson, The physics of debris flows, Rev. Geophys. 35 (3) (1997) 245–296.
[33] T. Takahashi, D.K. Das, Debris Flow: Mechanics, Prediction and Countermeasures, CRC Press, 2014.
[34] C.K.K. Lun, Kinetic theory for granular flow of dense, slightly inelastic, slightly rough spheres, J. Fluid Mech. 233 (1991) 539–559.
[35] J. Jung, D. Gidaspow, I.K. Gamwo, Measurement of two kinds of granular temperatures, stresses, and dispersion in bubbling beds, Ind. Eng. Chem. Res. 44 (5) (2005) 1329–1341.
[36] H. Yang, Y. Zhu, R. Li, Q. Sun, Kinetic granular temperature and its measurement using speckle visibility spectroscopy, Particuology 48 (2020) 160–169.
[37] D.J. Holland, C.R. Müller, J.S. Dennis, L.F. Gladden, A.J. Sederman, Spatially resolved measurement of anisotropic granular temperature in gas-fluidized beds, Powder Technol. 182 (2) (2008) 171–181.
[38] A. Penn, T. Tsuji, D.O. Brunner, C.M. Boyce, K.P. Pruessmann, C.R. Müller, Real-time probing of granular dynamics with magnetic resonance, Sci. Adv. 3 (9) (2017), e1701879, .
[39] R.M. Iverson, D.L. George, Modelling landslide liquefaction, mobility bifurcation and the dynamics of the 2014 Oso disaster, Géotechnique 66 (3) (2015) 175–187.
[40] S.P. Pudasaini, M. Mergili, A multi-phase mass flow model, J. Geophys. Res. 124 (12) (2019) 2920–2942.
[41] P.A. Cundall, O.D. Strack, A discrete numerical model for granular assemblies, Géotechnique 29 (1) (1979) 47–65.
[42] K. Soga, E. Alonso, A. Yerro, K. Kumar, S. Bandara, Trends in large-deformation analysis of landslide mass movements with particular emphasis on the material point method, Géotechnique 66 (3) (2016) 248–273.
[43] J.J. Monaghan, Smoothed particle hydrodynamics, Rep. Prog. Phys. 68 (8) (2005) 1703.
[44] Z. Han, B. Su, Y. Li, W. Wang, W. Wang, J. Huang, G. Chen, Numerical simulation of debris-flow behavior based on the SPH method incorporating the Herschel-Bulkley-Papanastasiou rheology model, Eng. Geol. 255 (2019) 26–36.
[45] W. Wang, G. Chen, Z. Han, S. Zhou, H. Zhang, P. Jing, 3D numerical simulation of debris-flow motion using SPH method incorporating non-Newtonian fluid behavior, Nat. Hazards 81 (3) (2016) 1981–1998.
[46] J. Zhao, T. Shan, Coupled CFD-DEM simulation of fluid–particle interaction in geomechanics, Powder Technol. 239 (2013) 248–258.
[47] X. Li, J. Zhao, Dam-break of mixtures consisting of non-Newtonian liquids and granular particles, Powder Technol. 338 (2018) 493–505.
[48] A. Leonardi, F.K. Wittel, M. Mendoza, R. Vetter, H.J. Herrmann, Particle-fluid-structure interaction for debris flow impact on flexible barriers, Comput. Aid. Civ. Inf. Eng. 31 (5) (2016) 323–333.
[49] W.J. Xu, X.Y. Dong, W.T. Ding, Analysis of fluid-particle interaction in granular materials using coupled SPH-DEM method, Powder Technol. 353 (2019) 459–472.
[50] T. Shan, J. Zhao, A coupled CFD-DEM analysis of granular flow impacting on a water reservoir, Acta Mech. 225 (8) (2014) 2449–2470.
[51] Y. Kong, J. Zhao, X. Li, J.S.H. Kwan, E.C.H. Sze, Coupled CFD/DEM modeling of multiphase debris flow over a natural erodible terrain: the Yu Tung Road case, Proceedings of the Second JTC1 Workshop on Triggering and Propagation of Rapid Flow-like Landslides, Hong Kong 2018, pp. 197–200.
[52] X. Li, J. Zhao, A unified CFD-DEM approach for modeling of debris flow impacts on flexible barriers, Int. J. Numer. Anal. Methods Geomech. 42 (14) (2018) 1643–1670.
[53] X. Li, J. Zhao, K. Soga, A new physically based impact model for debris flow, Géotechnique (2020) 1–12.
[54] T.B. Anderson, R. Jackson, Fluid mechanical description of fluidized beds. Equations of motion, Ind. Eng. Chem. Fundam. 6 (4) (1967) 527–539.
[55] J.U. Brackbill, D.B. Kothe, C. Zemach, A continuum method for modeling surface tension, J. Comput. Phys. 100 (2) (1992) 335–354.
[56] V.W.H. Herschel, Consistency of measurements rubber-benzene solutions, Kolloid-Zeit. 39 (1926) 291–300.
[57] J.F. Steffe, Rheological Methods in Food Process Engineering, Freeman Press, 1996.
[58] Y. Tsuji, T. Tanaka, T. Ishida, Lagrangian numerical simulation of plug flow of cohesionless particles in a horizontal pipe, Powder Technol. 71 (3) (1992) 239–250.
[59] Z.Y. Zhou, S.B. Kuang, K.W. Chu, A.B. Yu, Discrete particle simulation of particle–fluid flow: model formulations and their applicability, J. Fluid Mech. 661 (2010) 482–510.
[60] K.D. Kafui, C. Thornton, M.J. Adams, Discrete particle-continuum fluid modelling of gas–solid fluidised beds, Chem. Eng. Sci. 57 (13) (2002) 2395–2410.
[61] R. Di Felice, The voidage function for fluid-particle interaction systems, Int. J. Multiphase Flow 20 (1) (1994) 153–159.
[62] H.G. Weller, G. Tabor, H. Jasak, C. Fureby, A tensorial approach to computational continuum mechanics using object-oriented techniques, Comput. Phys. 12 (6) (1998) 620–631.
[63] C. Kloss, C. Goniva, Liggghts: a new open source discrete element simulation software, Proceedings of The Fifth International Conference on Discrete Element Methods, London, UK 2010, pp. 25–26.
[64] C. Goniva, C. Kloss, A. Hager, S. Pirker, An open source CFD-DEM perspective, Proceedings of OpenFOAMWorkshop, Göteborg 2010, pp. 1–10.
[65] A. Remaître, J.P. Malet, O. Maquaire, C. Ancey, J. Locat, Flow behaviour and runout modelling of a complex debris flow in a clay-shale basin, Earth Surf. Process Land. 30 (4) (2005) 479–488.
[66] E.M. Smuts, D.A. Deglon, C.J. Meyer, Methodology for CFD-DEM modelling of particulate suspension rheology, Proceedings of the Ninth International Conference on CFD in the Minerals and Process Industries CSIRO, Melbourne, Australia 2012, pp. 37–53.
[67] D. Song, Mechanisms of Debris Flow Impact on Rigid and Flexible Barriers, Ph.D. thesis The Hong Kong University of Science and Technology, Hong Kong, China, 2016.
[68] R. Delannay, A. Valance, A. Mangeney, O. Roche, P. Richard, Granular and particle-laden flows: from laboratory experiments to field observations, J. Phys. D 50 (5) (2017), 053001, .
[69] Y. Duan, Z.G. Feng, E.E. Michaelides, S. Mao, Modified kinetic theory applied to the shear flows of granular materials, Phys. Fluids 29 (4) (2017), 043302, .
[70] D.M. Hanes, O.R. Walton, Simulations and physical measurements of glass spheres flowing down a bumpy incline, Powder Technol. 109 (1–3) (2000) 133–144.
[71] R. Delannay, M. Louge, P. Richard, N. Taberlet, A. Valance, Towards a theoretical picture of dense granular flows down inclines, Nat. Mater. 6 (2) (2007) 99.
[72] P.H. Law, Computational Study of Granular Debris Flow Impact on Rigid Barriers and Baffles, Ph.D. thesis The Hong Kong University of Science and Technology, Hong Kong, China, 2014 251–252.

[73] M. Torrilhon, H. Struchtrup, Regularized 13-moment equations: shock structure calculations and comparison to Burnett models, J. Fluid Mech. 513 (2004) 171–198.
[74] F.J. Uribe, Shock waves: the Maxwell-Cattaneo case, Phys. Rev. E 93 (3) (2016), 033110, .
[75] M.D. Ediger, Spatially heterogeneous dynamics in supercooled liquids, Annu. Rev. Phys. Chem. 51 (1) (2000) 99–128.
[76] L. Piñeiro, M. Novo, W. Al-Soufi, Fluorescence emission of pyrene in surfactant solutions, Adv. Colloid Interf. Sci. 215 (2015) 1–12.
[77] B. Schmidt, Electron beam density measurements in shock waves in argon, J. Fluid Mech. 39 (2) (1969) 361–373.
[78] P. Wang, C. Song, C. Briscoe, K. Wang, H.A. Makse, From force distribution to average coordination number in frictional granular matter, Phys. A Stat. Mech. Appl. 389 (19) (2010) 3972–3977.
[79] L.L. Yang, J.J. Padding, J.H. Kuipers, Modification of kinetic theory of granular flow for frictional spheres, part I: two-fluid model derivation and numerical implementation, Chem. Eng. Sci. 152 (2016) 767–782.
[80] D.J. Parker, Positron emission particle tracking and its application to granular media, Rev. Sci. Instrum. 88 (5) (2017), 051803, .
[81] W.S. Chepil, N.P. Woodruff, The physics of wind erosion and its control, Adv. Agron, 15, Academic Press 1963, pp. 211–302.
[82] J. Fang, L.Z. Wang, Y. Hong, J.D. Zhao, Influence of solid-fluid interaction on impact dynamics against rigid barrier: CFD-DEM modelling, Géotechnique (2021) 1–62.
[83] C. Wendeler, A. Volkwein, B.W. McArdell, P. Bartelt, Load model for designing flexible steel barriers for debris flow mitigation, Can. Geotech. J. 56 (6) (2019) 893–910.